Remote Sensing of Environment 341 (2026) 115453

Contents lists available at ScienceDirect

Remote Sensing of Environment

journal homepage: www.elsevier.com/locate/rse

Hyperspectral constraints reduce bias in ECOSTRESS evapotranspiration and drought indicators☆

Michael Marshall [a,*], Monica Pepe [b], Giulia Tagliabue [c], Vincent Odongo [d], Wim Timmermans [a], Francesco Vuolo [e], Agnieszka Soszynska [f], Kwasi Ofori-Karikari [g], Egor Prikaziuk [a], Volkan Yilmaz [a,h], Serkan Girgin [a], Cinzia Panigada [c], Micol Rossini [c], Francesco Fava [i], Sonja M. Leitner [d], Christoph Hecker [a], Lutz Merbold [j], Zoltan Szantoi [k,l], Mirco Boschetti [b]

[a] Faculty of Geo-Information Science and Earth Observation, University of Twente, Hallenweg 8, 7522NH Enschede, the Netherlands
[b] Institute for Electromagnetic Sensing of the Environment, Italian National Research Council, Via Bassini 15, 20133, Milan, Italy
[c] Department of Earth and Environmental Sciences, University of Milano – Bicocca, Piazza della Scienza 1, 20126, Milan, Italy
[d] Mazingira Centre for Environmental Research and Education, International Livestock Research Institute (ILRI), Naivasha Rd, PO 30709, 00100 Nairobi, Kenya
[e] Institute of Geomatics, BOKU University, Peter-Jordan-Straße 82, 1190 Vienna, Austria
[f] National Centre for Earth Observation (NCEO), Earth Observation Science, Department of Physics & Astronomy, University of Leicester, LE1 7RH Leicester, UK
[g] Università Cattolica del Sacro Cuore, Largo A. Gemelli 1, 20123 Milan, Italy
[h] Department of Geomatics Engineering, Faculty of Engineering, Karadeniz Technical University, 61080 Trabzon, Turkey
[i] Department of Environmental Science and Policy, Università degli Studi di Milano, Via Celoria 2, 20133 Milan, Italy
[j] Integrative Agroecology Group, Research Division Agroecology and Environment, Agroscope, Reckenholzstr. 191, 8046 Zurich, Switzerland
[k] Science, Applications & Climate Department, European Space Agency, Frascati, Italy
[l] Department of Geography and Environmental Studies, Stellenbosch University, Stellenbosch, South Africa

ARTICLE INFO

Edited by Marie Weiss

Keywords:
Drylands
Evaporative stress index
Evapotranspiration partitioning
Soil evaporation
PT-JPL
Imaging spectroscopy
PRISMA
EnMAP

ABSTRACT

Droughts in Africa's drylands threaten regional food security and global agricultural markets. Early-warning systems increasingly rely on Earth Observation (EO), yet precipitation-based indicators often fail to detect emerging vegetation water stress. With new low-Earth-orbit missions, evapotranspiration (ET), which represents actual land-surface water flux, and ET-derived metrics such as the Evaporative Stress Index (ESI) have become essential. ECOSTRESS provides ~70 m sub-daily land surface temperature observations for ET estimation via the Priestley–Taylor Jet Propulsion Laboratory (PT-JPL) model. However, PT-JPL often exhibits positive ET bias in drylands, increasing the risk of drought omission errors. We evaluated whether hyperspectral vegetation indices (HVIs) can reduce these biases using multi-year field spectrometry, eddy covariance fluxes, and EnMAP/PRISMA imagery in a Kenyan dryland experiment. On the independent validation subset, the standard PT-JPL overestimated ET by 21.8% (mean observed latent heat = 4.86 MJ m^{-2} d^{-1}). Incorporating HVIs reduced bias to 3.5% when constraining soil evaporation and to −6.4% when applied to both canopy and soil components, while also improving other goodness-of-fit metrics. Bias reduction occurred through two mechanisms: (i) alleviating NDVI saturation, which strengthened canopy constraints under wetter conditions, and (ii) reformulating the soil-moisture constraint using hyperspectral reflectance, thereby limiting soil-evaporation inflation under humid and transitional conditions. These improvements were consistent across hydrological periods and sensor platforms. The findings demonstrate that narrowband spectral information enhances ET partitioning and directly support upcoming narrowband–thermal missions (e.g., CHIME, Landsat Next, LSTM, S2NG, SBG) by improving ET-based drought early-warning in moisture-limited environments.

☆ This article is part of a Special issue entitled: 'Remote Sensing in Ecohydrology' published in Remote Sensing of Environment.

* Corresponding author.
E-mail address: m.t.marshall@utwente.nl (M. Marshall).

https://doi.org/10.1016/j.rse.2026.115453
Received 28 November 2025; Received in revised form 16 April 2026; Accepted 24 April 2026
Available online 30 April 2026

1. Introduction

Droughts in dryland agroecosystems arise from below-normal rainfall and elevated atmospheric moisture demand, which can decouple vegetation water demand from meteorological supply and intensify evapotranspiration (ET) losses and soil moisture depletion (West et al., 2019). Over one or multiple growing seasons, these dynamics reduce agricultural production and increase food insecurity. The 2020–2023 Horn of Africa drought, following flooding in 2019–2020, left more than 30 million people acutely food insecure (OCHA, 2023), underscoring the need for drought-resilient agroecosystems. Monitoring systems such as the Famine Early Warning Systems Network (FEWS NET) integrate satellite and geospatial information to provide timely assessments of drought severity, extent, and risk (Funk et al., 2019).

Drought monitoring in Africa's drylands traditionally relied on coarse (>1 km) spatial resolution imagery acquired by geostationary weather satellites (Funk et al., 2015) and precipitation-based indices such as the Standardized Precipitation Index (SPI) (McKee, 1993). While useful for characterizing drought onset, SPI often fails to capture the full extent of water stress experienced by vegetation and agroecosystems over prolonged dry periods. Despite rainfall recovery in parts of Africa's drylands in the 1990s, ET anomalies increasingly showed negative departures from the long-term mean, which is indicative of drought development (Marshall et al., 2012). In a process referred to as *aridity intensification*, warming conditions elevate vapor pressure deficit and atmospheric moisture demand, driving vegetation and soil moisture losses even when precipitation is near normal (Zhou et al., 2019). Rising temperatures may further accelerate soil evaporation and reduce the fraction of rainfall available for plant growth (Hobbins et al., 2016; Lian et al., 2021). Consequently, precipitation alone may become an unreliable indicator of drought. To illustrate how this decoupling manifests at the local scale, we show a Water Productivity through Open Access of Remotely sensed derived data (WaPOR) (FAO, 2020)–derived ET and precipitation time series for the Kapiti Research Station & Wildlife Conservancy (Fig. S1), which highlights periods during the recent Horn of Africa drought when near- or above-average precipitation coincided with inhibited ET.

Because precipitation alone may not capture vegetation water stress, ET-based diagnostics have gained prominence, though their accuracy depends strongly on how surface energy balance and vegetation processes are represented in remote sensing models (Fisher et al., 2017). Accurate estimation of ET requires finer spatial and spectral resolution than weather satellites afford, because ET is sensitive to variations in canopy structure, physiology, and surface–atmosphere coupling (Anderson et al., 2011). The emergence of low-Earth-orbit satellite imagery, including Landsat-class observations, enabled the development of ET-based drought indices such as Evaporative Stress Index (ESI). ESI represents standardized anomalies of the ratio between actual ET and reference (ET_0, the atmospheric evaporative demand over a well-watered reference surface), rather than standardized anomalies of ET alone (Anderson et al., 2007). By normalizing ET with atmospheric evaporative demand, ESI isolates soil-moisture-driven stress signals from purely meteorological forcing.

Ecosystem Spaceborne Thermal Radiometer Experiment on Space Station (ECOSTRESS) deployed on the International Space Station in 2018, provides high-resolution (~70 m) thermal infrared observations at varying local overpass times, enabling improved diurnal characterization of land surface temperature and ET (Fisher et al., 2020). ECOSTRESS serves as an experimental precursor to the upcoming Copernicus Land Surface Temperature Monitoring (LSTM) mission, which aims to operationalize thermal infrared (TIR) retrievals to support ET and ESI estimation for improved field-scale drought monitoring and water management worldwide (Bernard et al., 2023). The NASA ECOSTRESS mission produces ET and ESI with the Atmosphere–Land Exchange Inverse (ALEXI) (Anderson et al., 2007) and Priestley–Taylor Jet Propulsion Laboratory (PT-JPL) (Fisher et al., 2008) models, with PT-JPL serving as the mission-standard algorithm. PT-JPL generally performs well across ecosystems due to its parsimonious structure and low error propagation (Ershadi et al., 2014; Michel et al., 2016) and has been incorporated into ET benchmarks such as WACMOS-ET and OpenET (Melton et al., 2022; Miralles et al., 2016). However, this same parsimony introduces structural rigidity, limiting the model's ability to adapt to site-specific soil evaporation dynamics in moisture-limited environments, particularly under conditions of high vapor pressure deficit and weak surface–atmosphere coupling (Marshall et al., 2020; Purdy et al., 2018).

Despite its broad applicability, the parsimonious structure of PT-JPL can lead to systematic ET overestimation in dryland ecosystems, particularly when atmospheric moisture conditions are decoupled from surface soil moisture availability (Hu et al., 2023; Liang et al., 2022). This bias arises mainly from its soil-evaporation component, which assumes that near-surface relative humidity reflects the equilibrium between surface moisture supply and atmospheric demand (i.e., potential evapotranspiration or PET) (Marshall et al., 2020). In drylands, the soil surface dries rapidly after rainfall, while the overlying atmosphere can remain relatively humid due to advection or transpiration. This decoupling causes PT-JPL to interpret atmospheric humidity as indicative of wet soils, inflating soil evaporation. Recent efforts have explored spectral constraints on soil evaporation with broadband shortwave infrared (SWIR), TIR, and microwave observations (García et al., 2013; Purdy et al., 2018; Zhang et al., 2021). These approaches provide valuable constraints on surface temperature and soil moisture, but remain indirect proxies of vegetation function and often lack sensitivity to canopy biochemical dynamics. In contrast, hyperspectral narrowbands (HNBs) resolve specific absorption features related to chlorophyll, water content, and canopy structure, enabling more direct representation of vegetation processes that regulate ET partitioning. The explicit parameterization of PT-JPL with hyperspectral HNBs has received little attention. An analysis involving field spectrometers shows promise, as hyperspectral vegetation indices (HVIs) improved transpiration and soil-evaporation estimates for irrigated croplands by 17% and 14%, respectively (Marshall et al., 2016). New hyperspectral missions such as EnMAP and PRISMA now provide on-demand global coverage at high spectral fidelity, providing an opportunity to evaluate whether HNBs can enhance ECOSTRESS PT-JPL ET estimation and drought monitoring via ESI in Africa's drylands.

This study evaluates whether HNBs improve ECOSTRESS PT-JPL ET partitioning and ESI using multi-year ground and satellite spectral observations at the Kapiti Research Station & Wildlife Conservancy in Kenya (https://www.ilri.org/research/facilities/kapiti-research-station-wildlife-conservancy). Ground-based instrumentation, including an autonomous field spectrometer and EC flux tower, were used to optimize the transpiration and soil evaporation components of PT-JPL with HVIs. The optimized model was then extended spatially across the Conservancy with EnMAP and PRISMA HVIs to assess spatial variability in model performance. We further examined whether bias reduction in ET improved the consistency of the derived ESI for drought detection. A second EC flux tower on a neighbouring farm allowed independent validation.

2. Study area

The main experimental setup was located in Kapiti, which is approximately 60 km from Nairobi in Machakos County, Kenya (Fig. 1). Kapiti spans an area roughly 130 km^2. It ranges in elevation from 1615 to 1920 m above sea level (UNEP, 2008). The annual average precipitation is approximately 550 mm with a bimodal rainfall pattern consisting of the long rains from March to May and the short rains from October to December. Interannual rainfall variability is high. Vegetation consists of grasslands, shrublands, and open savanna woodlands. Soils consist of Ferralsols and Luvisols on ridges, and Vertisols and Planosols in plains with patches of sandy alluvial deposits along ephemeral

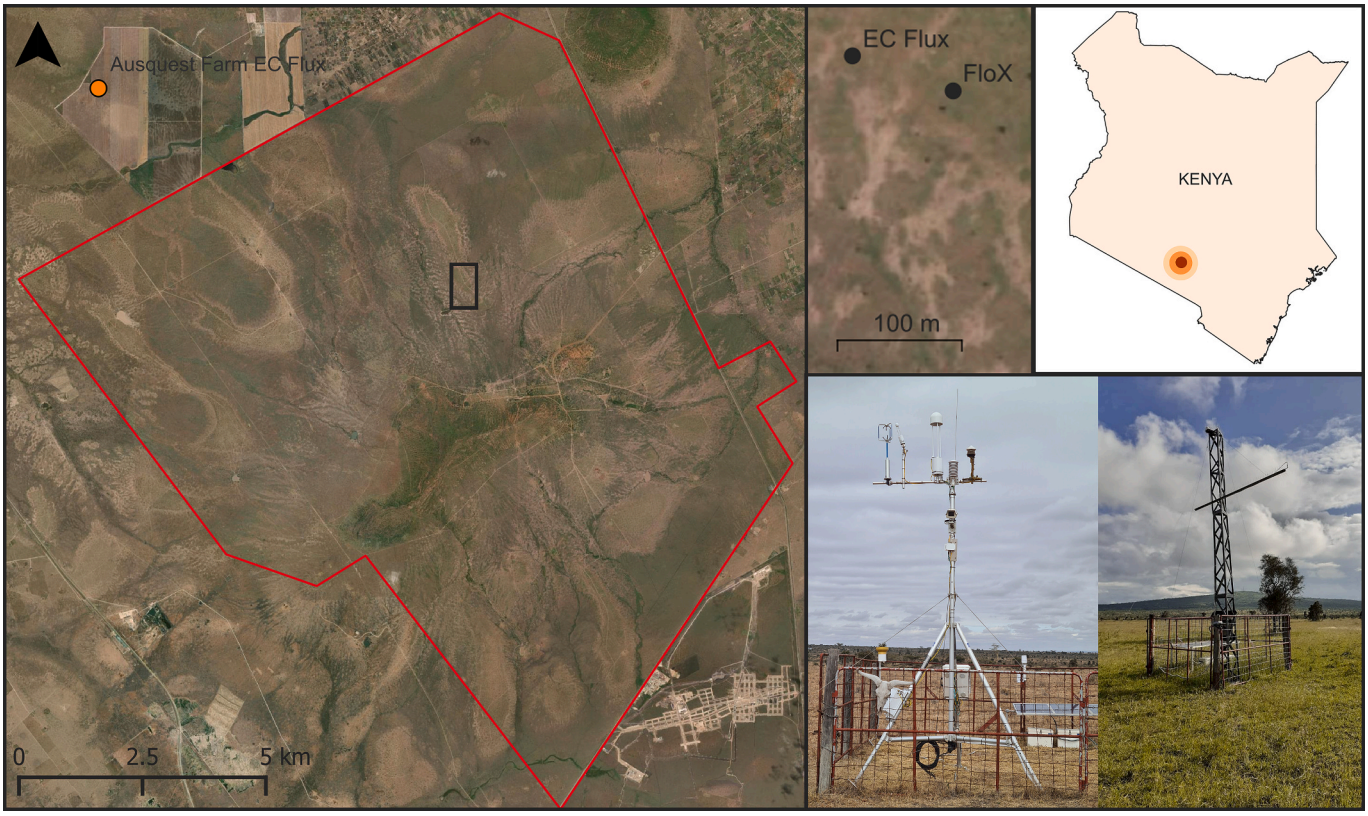

Fig. 1. Kapiti Research Station & Wildlife Conservancy and AusQuest Farm. The main experimental setup consisted of an EC flux tower (left) and FloX autonomous field spectrometer (right) within a 100 m flux footprint in the Kapiti. A second EC flux tower is located on the AusQuest farm for validation.

channels (Gachene et al., 2025). The combination of sparse to moderate vegetation cover, strong wet–dry seasonality, and limited soil moisture storage creates conditions in which ET is highly sensitive to atmospheric demand and vegetation state, making the site well suited for evaluating ET partitioning and drought processes in moisture-limited systems.

A flat open grassland portion of the station consisting of Vertisols has been equipped with permanent scientific instrumentation for remote sensing and ecological research. These include a LiCOR eddy covariance EC system with LI-7500DS Open-Path CO_2/H_2O gas analyzer at 5 m above the surface (Odongo et al., 2025) and Fluorescence Box (FloX, JB Hyperspectral Devices GmbH, Germany) autonomous field spectrometer on a 6 m tall optical observation tower (Wen et al., 2025). The spectrometer is positioned at 37°8.02′ E, 1° 36.87′ S, approximately 100 m southeast of the flux tower. The spectrometer is in the dominant southeasterly wind sector and intersecting the 40–50% climatological flux footprint isolines, as identified from footprint climatology analyses (Gachene et al., 2025). A second LiCOR EC system with a CO_2/H_2O gas analyzer mounted at 4 m above the surface was installed in a cultivated field at the AusQuest farm (37°4.05′ E, 1°34.68′ S). AusQuest is a large-scale commercial rainfed dryland farm on the northwest border of Kapiti that produces fodder crops for livestock and cultivates a range of pulses for seed production, including chickpeas and mung beans.

3. Material and methods

The assessment of the NASA ECOSTRESS ET and ESI workflow with HVIs consisted of three main phases: (i) optimization of the PT-JPL model using EC flux tower and FloX autonomous field spectrometer data collected at Kapiti; (ii) spatial application of the optimized PT-JPL across the Conservancy using EnMAP- and PRISMA-derived HVIs in combination with ECOSTRESS land surface temperature (LST) and ancillary geospatial data; and (iii) independent validation of the spatial ET against EC flux tower measurements from the AusQuest farm (Fig. S2).

3.1. Field data

The EC flux and FloX towers in Kapiti represent a unique experimental setup because they collect high-quality sub-daily micrometeorological and hyperspectral reflectance information on a rolling basis. The second EC flux tower was standalone, which is why it was only used for validation of the spatial ET and ESI products. The Kapiti experiment spanned nearly 1.5 years from 2019 to 2020 and 2023–2024. In between the two periods, the EC flux tower was decommissioned and the FloX tower was not regularly maintained because of travel restrictions during the COVID pandemic. Two new EC flux towers were installed and the FloX tower was refurbished at the beginning of 2023. The same EC instrumentation was used during both observation periods; however, the sensor height in Kapiti was slightly lower in the pre-COVID installation (4.33 m). The impact of the height differences is minimal given the low canopy height of the grassland (<1 m). Both heights sufficiently capture the fetch and fully developed turbulent mixing. Raw EC flux data were processed in LI-COR EddyPro® (v7.0.9) following standard procedures, including coordinate rotation and tilt correction after (McMillen, 1988), frequency response correction (Moore, 1986), density correction (Webb et al., 1980), spike detection following Vickers and Mahrt (1997), and overall flux processing frameworks and corrections described in Moncrieff et al. (1997). They were aggregated to a daily timestep over daylight hours to coincide with the FloX measurements. Coupling between the land surface and the boundary layer is also strongest during daytime making it an ideal period of day for simulating ET (Fisher et al., 2008). Daytime values were flagged with an incoming shortwave radiation threshold of $\geq$10 W m^{-2} (Hirschi et al., 2017). An energy imbalance on the order of 20% or more frequently exists because latent heat (LE) and sensible heat (H) are measured with different instruments (Wilson et al., 2002). We therefore used the Bowen ratio

method (Twine et al., 2000) to close the energy balance. Recent analyses indicate that no single closure approach is universally optimal; however, the Bowen ratio method tends to perform comparatively better under strongly convective daytime conditions when vertical transport dominates the imbalance (Zhou et al., 2023). Given the dry, sparsely vegetated, and well-mixed daytime boundary layer conditions at Kapiti, this approach was considered appropriate for our application. We note that any closure method introduces uncertainty, but because all model variants were evaluated against the same corrected flux dataset, relative performance comparisons remain robust.

The FloX system comprises two temperature-stabilized grating spectrometers (Ocean Insight, USA): a FLAME (400–950 nm, full width at half maximum-FWHM = 1.5 nm) for canopy reflectance and a QEPro (650–800 nm, full width at half maximum = 0.3 nm) for sun-induced chlorophyll fluorescence retrieval. Only reflectance data from the FLAME spectrometer were used in this study. Incoming irradiance and reflected radiance were measured via up- and down-looking optical fibers. The up-looking fibers were fitted with cosine receptors and positioned at the top of the tower to minimize shading. The down-looking bare fibers had a field of view of 25° and were positioned 4.5 m above ground level, corresponding to a footprint of 1.9 m diameter, which is considerably smaller than the EC flux footprint that integrates surface fluxes over hundreds of meters depending on atmospheric stability and wind conditions. Although this difference in sampling scale introduces some uncertainty, the relative uniformity of the grassland cover supports its use as a representative optical sampling location for model parameterization. The raw FloX data were converted from digital numbers to radiance with the calibration files of the spectrometer. Apparent reflectance was used for model parameterization. It was calculated as the ratio of upwelling radiance to downwelling irradiance divided by π. Low-quality measurements were discarded using quality flags. The filtering criteria were defined as follows: i) solar zenith angle $\leq 70°$; ii) percent difference between the irradiance measurement collected before and after each target measurement <1%; and iii) dynamic range > 60% and < 90%. After filtering, the reflectance spectra collected within ±2 h solar noon were extracted and averaged daily to minimize variations in landscape illumination and solar geometry. Finally, the reflectance spectra were truncated to the 400–930 nm range prior to analysis to exclude high-noise regions at the edges of the spectrometer's detection limits and retain only spectrally reliable bands for HVI optimization.

3.2. Earth observation and ancillary geospatial data

Our initial goal was to compare ET and ESI estimates driven by HVIs derived from both proximal sensing and Earth Observation (EO) data over the entire study period. However, two primary constraints limited the depth of the EO analysis, and the imagery was therefore used only for demonstration and partial validation. First, EnMAP and PRISMA are not fully operational missions; image acquisitions must be requested directly from the German and Italian space agencies. Acquisition frequency is constrained by satellite tasking priorities and orbital scheduling. Between 2019 and 2020, only one PRISMA scene was acquired over Kapiti, and it covered only part of the Conservancy, missing the EC flux-tower footprint. Although many EnMAP and PRISMA scenes were obtained from 2022 to 2024, most were unusable because of cloud cover, long revisit intervals, or incomplete spatial coverage. Consequently, two clear EnMAP–PRISMA pairs (23 February and 18 March 2023) were selected for the spatial analysis (Table 1). The "green-up" phase in 2023 began in mid-October following the onset of the short rainy season. Vegetation productivity peaked at the end of January. The image dates therefore correspond to the senescence period for vegetation in the footprints. At the time of analysis, the Level-3 ECOSTRESS ET and ESI data layers did not include forcing data. Additional geospatial datasets were therefore incorporated to address gaps in the ECOSTRESS processing workflow and to ensure performance was assessed purely on the integration of HVIs. ECOSTRESS LST, emissivity, and precipitable water vapor (PWV) data were combined with Landsat-8 (OLI) albedo to close the surface energy balance. Agrometeorological indicators from 1979 to the present, derived from reanalysis (AgERA; https://cds.climate.copernicus.eu/datasets/sis-agrometeorological-indicators?tab=overview) were used to estimate remaining energy and climate terms.

All EO data underwent further processing to insure geometric and radiometric consistency. The data were co-registered with the "AROSICS" package in Python (Scheffler et al., 2017), with Sentinel-2 imagery (WGS-84 UTM Zone 37S) serving as the geometric reference. The EO imagery were resampled to 30 m resolution with nearest neighbor. We chose to preserve the finer-scale optical variability rather than aggregate hyperspectral reflectance to ECOSTRESS (70 m) because spatial heterogeneity in ET across the Conservancy is primarily driven by vegetation structure and canopy function, which vary at sub-field scales, whereas thermal gradients were comparatively smooth. Resampling therefore ensured grid alignment without altering the integrated thermal signal or redistributing energy across pixels. We used the standard EnMAP Level-2 (bottom-of-atmosphere reflectance) and PRISMA Level-1 (geometrically corrected top-of-atmosphere radiance) data for the analysis. We did not use the standard Level-2 PRISMA product because of artificial spikes in the NIR and other noise in the data (Marshall et al., 2022). Atmospheric correction of Level-1 PRISMA was performed with Atmospheric and Topographic Correction (ATCOR) software (Richter and Schlapfer, 2023). ATCOR applies the MODTRAN radiative transfer model (RTM) to correct for atmospheric scattering, absorption, and illumination effects. ATCOR was parameterized with the view geometry retrieved from the PRISMA metadata and visibility estimates derived from MOD04 (aerosol optical thickness, aerosol type): https://modis.gsfc.nasa.gov/data/dataprod/mod04.php. The ECOSTRESS Level-2 LST, emissivity, and PWV data were obtained from the Application for Extracting and Exploring Analysis Ready Samples (AppEEARS) platform (https://appeears.earthdatacloud.nasa.gov/). AppEEARS enables the extraction of analysis-ready NASA Earth Observation products for user-defined coordinates or polygons. ECOSTRESS scenes with less than 20% cloud cover and acquisition dates closest to the EnMAP and PRISMA overpasses were selected for further scrutiny. Acquiring ECOSTRESS images near the hyperspectral acquisition dates minimizes temporal differences in surface and atmospheric conditions, as ET and LST can vary considerably over short time intervals. Two cloud free images were the best candidates: one acquired one day after the target date at 10:37 local time, close to the EnMAP and PRISMA overpass times, and another

Table 1
Characteristics of Earth Observation (EO) instruments used to map ET and ESI.

Instrument	EO-variable	Spectral range (nm)	Spectral resolution (nm)	Spatial resolution (m)	Acquisition dates
EnMAP	Surface reflectance	420–2450	6.5 (VNIR) 10 (SWIR)	30	23-Feb-2023
PRISMA		400–2500	10 (VNIR) 12 (SWIR)		18-Mar-2023
ECOSTRESS	LST and emissivity	8000–12,000	70–100	70	24-Feb-2023 12-Mar-2023
Landsat-8	Albedo	430–2290	15–30	30	20-Feb-2023 8-Mar-2023

acquired six days earlier in the late afternoon at 15:54. Landsat Level-2 data were obtained from the United States Geological Survey Earth Explorer (https://earthexplorer.usgs.gov/) closest to the EnMAP/PRISMA dates. The Landsat images were three and ten days before respectively. We calculated surface albedo (α) from the visible, NIR, and SWIR Landsat reflectance bands (ρ) 1–7 following Andres-Anaya et al. (2024):

$$\alpha = 0.078 + 0.076 \bullet \rho_1 + 0.591 \bullet \rho_2 + 1.935 \bullet \rho_3 - 0.492 \bullet \rho_4 - 0.324 \bullet \rho_5 + 1.816 \bullet \rho_6 - 2.193 \bullet \rho_7 \quad (1)$$

AgERA consists of meaningful inputs for agro-ecological models at a daily timestep from 1979 to present globally. It is aggregated from ECMWF ERA-5 hourly data and interpolated to a 0.1° (~10 km) grid with ECMWF's high-resolution atmospheric model. We extracted shortwave downwelling radiation, two meter relative humidity and temperature tiles over the study area for the EnMAP/PRISMA dates to complete the parameterization of PT-JPL. The AgERA variables were applied uniformly across each scene without spatial downscaling. Given the relatively homogeneous topography and the dominance of vegetation-driven heterogeneity at field scales, we assumed that sub-kilometre gradients in shortwave downwelling radiation, temperature, and humidity were negligible relative to spectral variability in canopy structure. This assumption is consistent with previous applications of PT-JPL in semi-arid systems, where vegetation heterogeneity was shown to dominate ET variability (Marshall et al., 2013).

3.3. PT-JPL model and optimization

We adopted the version of the PT-JPL model described in García et al. (2013), which was developed for arid regions. The main difference between this version and the original PT-JPL is that ET is equal to the sum of plant transpiration (ET_C) and soil evaporation (ET_S) only. Canopy moisture interception and evaporation considered in the original PT-JPL is not accounted for in this version of PT-JPL. This simplification is reasonable because canopy moisture interception and evaporation is significant in humid dense vegetation. PT-JPL assumes an equilibrium between ET and PET. The model modulates deviations from the ET-PET equilibrium with a series of constraints (Table 2). Vegetation controls (f_{APAR}, f_{IPAR}) are derived from broadband NDVI, and the soil-moisture constraint (f_{SM}) is parameterized from near-surface relative humidity (RH) and vapor pressure deficit (VPD). These assumptions implicitly link canopy and soil processes to atmospheric state rather than to surface biochemical or biophysical properties. PET is estimated with the Priestley and Taylor (1972) simplification, which assumes PET is driven by available energy (net radiation minus soil heat flux, R_N - G) in MJ m^{-2} d^{-1} under constant advection (α_{PT} = 1.26). The available energy is further regulated by a weighting factor that is calculated from the slope of the saturation vapor pressure curve (Δ) (kPa $°C^{-1}$) and the psychrometric constant (γ), which is equal to 0.066 kPa $°C^{-1}$. The simplification reduces uncertainty compared to more complex formulations that incorporate aerodynamic and stomatal resistance (Ershadi et al., 2014).

$$ET = ET_C + ET_S = f_G f_T f_M \bullet \alpha_{PT} \bullet (\Delta/(\Delta+\gamma))R_{NC} + f_{SM} \bullet \alpha_{PT} \bullet (\Delta/(\Delta+\gamma))(R_{NS} - G) \quad (2)$$

In drylands, f_{APAR}, f_{IPAR}. and f_{SM} can become structurally weak: NDVI saturates under moderate-to-dense canopies, reducing sensitivity to incremental increases in canopy greenness, while RH/VPD may remain elevated even when the soil surface is moisture-limited. The hyperspectral optimization introduced here directly targets these two structural limitations.

The model was driven by EC flux and FloX tower data for simulations involving the PT-JPL formulation optimized with HVIs. A PT-JPL run with the NDVI (NIR – red / red + NIR) formulations was also performed for comparison purposes. The HNBs were spectrally resampled to match the MODIS Red (620–670 nm) and NIR (841–876 nm) broadbands to calculate NDVI, as PT-JPL was originally parameterized with MODIS NDVI. For the HVI-optimized runs, f_{APAR} and f_{IPAR}, the two principal spectral terms, were reformulated. Rather than prescribing broadband NDVI as the sole vegetation proxy, we allowed narrowband reflectance pairs to define data-driven HVIs that maximize sensitivity to observed ET dynamics. This effectively replaces the broadband structural proxy with physiologically sensitive spectral features in the green, red-edge, and NIR domains. HVIs were data-driven optimized narrowband normalized difference indices rather than predefined vegetation indices. For each simulation, a normalized difference ratio in the form (ρλ1 − ρλ2) / (ρλ1 + ρλ2), where λ1 and λ2 represent FloX narrowband reflectance, was computed from a given pair of HNBs, and the parameters m_1, b_1, m_2, and b_2 were re-calibrated with the Levenberg–Marquardt non-linear fitting algorithm (Elzhov et al., 2015). The algorithm was initialized with the original parameter values with a maximum of 1000 iterations. F_{APAR} and F_{IPAR} were bounded 0–1 because they are scalars. Mechanistically, this modification increases sensitivity to chlorophyll concentration, pigment dynamics, and canopy structure that are not fully captured by broadband NDVI, thereby reducing premature saturation of f_{APAR} and improving partitioning of available energy to ET_C. Optimization of ET_S via f_{SM} was more straightforward, as a new formulation replaced the RH and VPD equation based on Bouchet's hypothesis (Bouchet, 1963), to accommodate spectral information. This reformulation replaces the atmospheric proxy (RH/VPD) with a reflectance-based proxy more directly linked to surface moisture status, non-photosynthetic vegetation, and exposed soil background. In moisture-limited environments, soil surfaces often dry faster than the overlying air mass, creating a decoupling that can inflate ET_S in the original PT-JPL. The HVI-based f_{SM} is intended to reduce this inflation by tying the constraint to surface optical properties rather than boundary-layer humidity alone. Following García et al. (2013), who assessed the role of soil water content and apparent thermal inertia in estimating the soil moisture constraint, f_{SM} was defined as a scaled HVI:

Table 2
PT-JPL model parameters and equations. T_{OPT} is the optimum temperature for plant growth (25 °C), T_A is the daily mean air temperature (°C), PAR is photosynthetically active radiation, $f_{APAR,max}$ is the maximum f_{APAR} over a growing season, RH is relative humidity, and VPD is vapor pressure deficit (kPa). m_1, b_1, m_2, and b_2 are NDVI modifiers equal to 1.16, −0.14, 1.0, and − 0.05. Additional constants include: k_{PAR} = 0.5 (Ross, 1976), k_{RN} = 0.6 (Impens and Lemeur, 1969), and $\mathscr{6}$ = 1.0 kPa.

Variable	Description	Equation	Reference
f_G	Green canopy fraction	f_{APAR}/f_{IPAR}	Fisher et al. (2008)
f_T	Plant temperature constraint	$1.1814 \cdot [1 + e^{0.2 \cdot (Topt-10-TA)}]^{-1} \cdot [1 + e^{0.3 \cdot (-Topt-10-TA)}]^{-1}$	Potter et al. (1993)
f_M	Plant moisture constraint	$f_{APAR}/f_{APAR,max}$	Fisher et al. (2008)
f_{SM}	Soil moisture constraint	$RH^{VPD/\mathscr{6}}$	Fisher et al. (2008)
f_{APAR}	PAR fraction absorbed by green vegetation	$m_1 \cdot NDVI + b_1$	Myneni and Williams (1994)
f_{IPAR}	PAR fraction intercepted by total vegetation	$m_2 \cdot NDVI + b_2$	Fisher et al. (2008)
f_C	Fractional vegetation cover	f_{IPAR}	Campbell and Norman (1998)
LAI	Leaf area index	$-\ln(1 - f_C)/k_{PAR}$	Ross (1976)
R_{NS}	Net radiation (soil)	$R_N \cdot e^{(-krn \cdot LAI)}$	Fisher et al. (2008)
R_{NC}	Net radiation (canopy)	$R_N - R_{NS}$	Fisher et al. (2008)

$$f_{SM} = \frac{HVI - HVI_{min}}{HVI_{max} - HVI_{min}} \quad (3)$$

where HVI is the normalized difference ratio computed from a pair of given HNBs, HVI_{min} is the minimum value, and HVI_{max} is the maximum value over the available multi-year time series. Though suitable for retrospective analysis, this approach assumes knowledge of the full temporal range and would require climatological or rolling-window normalization for real-time implementation. As with f_{APAR} and f_{IPAR}, 1000 iterations of the Levenberg–Marquardt fitting algorithm were performed for optimization and F_{SM} was bounded 0–1.

To reduce the risk of overfitting and parameter interaction, ET_C was optimized first and ET_S parameters were subsequently optimized using the residual structure after canopy calibration. This sequential strategy reflects the physical hierarchy of the system: canopy transpiration typically explains the majority of ET variability, and errors in ET_C propagate directly into the residual available energy assigned to ET_S (Jasechko et al., 2013). Optimizing ET_C first therefore stabilizes the partitioning before recalibrating soil evaporation. Simultaneous optimization of both components led to non-convergence, indicating parameter interdependence. Optimization was stratified by high- and low-LE conditions spanning both hydrological periods to ensure robustness across moisture regimes and to reduce sensitivity to period-specific climatic anomalies. This stratified approach yielded more stable parameter estimates than calibrating on individual years separately.

3.4. Scaling out optimized PT-JPL with EnMAP and PRISMA HVIs

Some modifications to the R_N computation were needed to calculate pixelwise ET and ESI with the optimized and original ECOSTRESS workflows. R_N is calculated as the sum of net shortwave and longwave radiation:

$$R_N = (R_{SD} - R_{SU}) + (R_{LD} - R_{LU}) \quad (4)$$

R_{SD} represents daily average shortwave downwelling radiation (MJ m^{-2} d^{-1}), while shortwave upwelling radiation (R_{UD}) is calculated as a function of R_{SD} and scaled by α:

$$R_{SU} = \alpha R_{SD} \quad (5)$$

Longwave downwelling radiation (R_{LD}) is a function of the Stefan-Boltzmann constant ($\sigma = 5.67 \cdot 10^{-8}$ W m^{-2} K^{-4}), atmospheric emissivity (ε_A), and T_A in Kelvin:

$$R_{LD} = \sigma \varepsilon_A T_A^4 \quad (6)$$

ε_A is derived from PWV (ξ) in cm (Prata, 1996):

$$\varepsilon_A = 1 - (1 + \xi) e^{\left(-(C + D \bullet \xi)^{0.5}\right)} \quad (7)$$

Where C and D are constants equal to 1.2 and 3.0. Longwave upwelling radiation (R_{LU}) is also calculated with Stefan-Boltzmann's Law. Emissivity and temperature however are calculated at the surface. Surface emissivity (ε_S) and land surface temperature (T_S) are derived from emissivity and LST:

$$R_{LU} = \sigma \varepsilon_S T_S^4 \quad (8)$$

α and ε_S do not vary appreciably over the course of the day, but LST and PWV exhibit clear diurnal cycles (Sharifnezhadazizi et al., 2019; Wang et al., 2016). Therefore, the morning and late-afternoon ECOSTRESS overpasses do not represent the average daily conditions under which the energy balance is parameterized with AgERA R_{SD}. We applied empirical first-order adjustments to reduce this temporal mismatch. For the morning overpass, LST was reduced by 7 °C and PWV increased by 5%. For the late-afternoon overpass, LST was increased by 4 °C and PWV reduced by 5%. These scene-wide adjustments approximate daily mean conditions by accounting for the tendency of morning LST to exceed and afternoon LST to fall below daily mean values, while PWV typically increases during the day with boundary layer growth and surface moisture fluxes. Although this approach does not explicitly resolve surface-type differences in diurnal heating and cooling, it preserves spatial temperature gradients and was applied identically to both the standard and HVI-optimized PT-JPL configurations; therefore, any residual bias does not affect their comparative evaluation.

3.5. Quantitative analysis

We used standard performance metrics (R^2, RMSE, nRMSE, MBE) to optimize the PT-JPL model with field data and to validate the spatial version of the optimized model driven by EnMAP and PRISMA HVIs. The field data were split 60–40% between optimization and testing, with stratified sampling to balance the proportion of high (≥5 MJ m^{-2} d^{-1}) and low (<5 MJ m^{-2} d^{-1}) ET values. Validation of the spatial ET was limited to two EnMAP and PRISMA image pairs separated by 23 days. To estimate daily ET between the two hyperspectral acquisition dates, we linearly interpolated NDVI and the top-performing ET_C and ET_S HVIs as temporal scaling factors. These interpolated indices were not treated as new hyperspectral observations, but rather as a smooth transition between the two measured states to enable continuous PT-JPL simulations for comparison purposes. Although vegetation responses in drylands can exhibit nonlinear green-up following rainfall pulses, the interpolation was applied over a relatively short interval near the end of the growing season and was intended to approximate first-order temporal evolution rather than resolve peak phenological dynamics. Similar linear approaches are commonly used when combining 8- or 16-day MODIS vegetation indices with daily meteorological data (Fisher et al., 2008). The spatial ET and derived ESI were evaluated visually and compared using histograms.

4. Results

4.1. PT-JPL optimization

We first optimized the PT-JPL model using high-frequency EC flux and FloX spectral data from the Kapiti site to identify HVIs most sensitive to ET. The calibration statistics reflect the sensitivity of narrowbands to canopy and soil processes at this site; model generalizability is assessed in the independent testing and cross-site validation results. As expected for calibration, the optimization produced strong correlations and low errors (nRMSE ~0.22) across much of the visible and NIR, with rapid convergence (typically <1000 iterations). Correlations were slightly higher and errors lower for HNB-driven ET_C than for ET_S. The λ–λ plots (Figs. 2a & 3a) illustrate the pairwise R^2 values for HNBs optimized as normalized difference ratios for ET_C and ET_S. The highest-correlated HVIs for ET_C consisted of HNBs near the green peak (~550 nm) and across the NIR, with the highest-performing HVI defined by reflectance at 588.83 nm and 896.17 nm (FWHM ≈ 1.5 nm) ($R^2 = 0.92$, RMSE = 1.12 MJ m^{-2} d^{-1}). The calibration coefficients for this HVI (m_1, b_1, m_2, b_2) were 1.78, 0.67, 0.88, and 0.00, for F_{APAR} and F_{IPAR} computation, respectively. The highest-performing ET_S HVIs also drew from across the NIR but were centered at longer wavelengths in the red-edge to early NIR transition (680–730 nm), with the best combination defined by reflectance at 688.09 nm and 896.17 nm (FWHM ≈ 1.5 nm) (R^2 = 0.91, RMSE = 1.22 MJ m^{-2} d^{-1}). The density plots (Figs. 2b & 3b) encapsulate all HNBs contributing to HVIs with $R^2 \geq 0.7$ and therefore represent important but not necessarily the best performing pairs for ET_C and ET_S. HVIs including visible blue HNBs also contributed to the optimization of both ET_C and ET_S, potentially due to the contrast between soil and vegetation in the blue band. The visible green region contributed less to ET_S performance. Improvements from HVIs incorporating NIR narrowbands tapered off at the longest wavelengths, possibly due to sensor limits even after truncation. Many high-performing ET_C HVIs included red-edge HNBs but excluded other red HNBs strongly affected by chlorophyll absorption and prone to

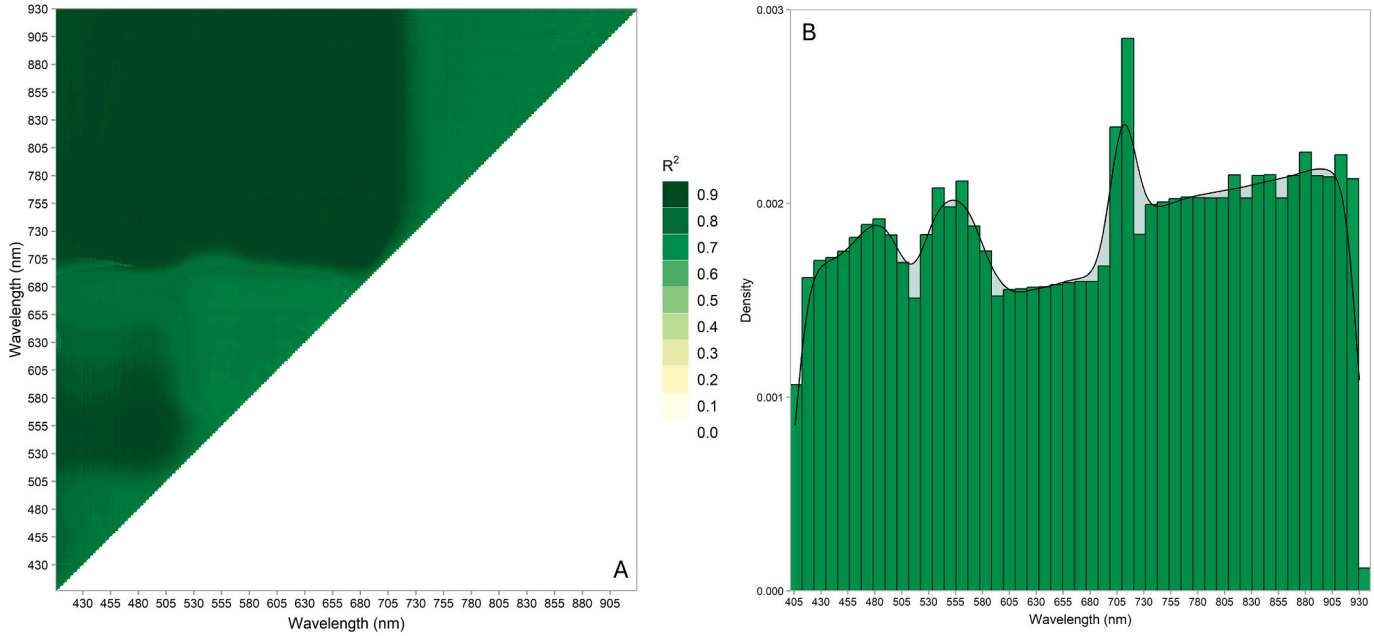

Fig. 2. Lambda-lambda (A) and density plots (B) illustrating the optimization performance of HNBs as normalized difference ratios in the PT-JPL model for ET_C.

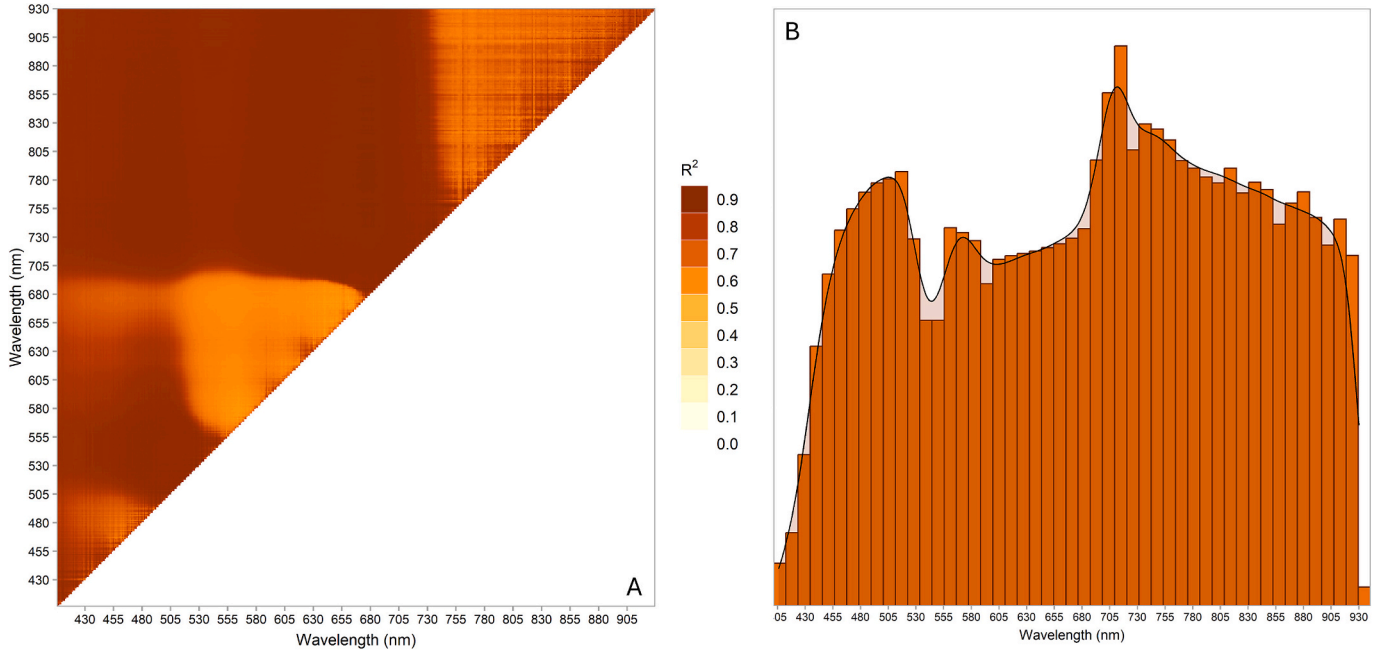

Fig. 3. Lambda-lambda (A) and density plots (B) illustrating the optimization performance of HNBs as normalized difference ratios in the PT-JPL model for ET_S.

saturation.

In a separate analysis, we evaluated ET estimates from the TSEB model (Norman et al., 1995) driven by the EC flux micrometeorological data and FloX HNBs. Following Richter and Timmermans (2009), HNBs were input to a PROSAIL RTM (Jacquemoud, 1993) to estimate vegetation fraction, the primary optical EO variable in TSEB. We compared LAI derived from PROSAIL with LAI calculated with our HVI calibration coefficients to verify the consistency of the optimization and found strong agreement ($R^2 = 0.96$, RMSE = 0.17 m^2 m^{-2}).

We next evaluated PT-JPL performance using the highest-performing ET_C and ET_S HVIs against the original configuration parameterized with NDVI and RH/VPD (Fig. 4). Results are reported for the independent validation subset; calibration statistics are shown for reference only. The original PT-JPL performed reasonably well ($R^2 = 0.82$, RMSE = 1.74 MJ m^{-2} d^{-1}, nRMSE = 0.36) but exhibited a systematic positive bias of 1.06 MJ m^{-2} d^{-1}, corresponding to a 21.8% overestimation relative to the mean observed ET (4.86 MJ m^{-2} d^{-1}). Replacing only F_{SM} with the HVI-based formulation reduced bias to 3.5% while increasing R^2 by 0.06 and lowering RMSE by 0.31 MJ m^{-2} d^{-1}. Substituting only the canopy constraints in ET_C with the HVI formulation reduced bias to 11.2% and improved R^2 by 0.04. When both components were parameterized with HVIs, overall performance improved further ($R^2 = 0.88$, RMSE = 1.44 MJ m^{-2} d^{-1}, nRMSE = 0.30), and bias shifted slightly negative (−6.4%), indicating modest underestimation at higher ET. This fully HVI-driven configuration was used for subsequent spatial analysis to ensure internal consistency between canopy and soil constraints derived from

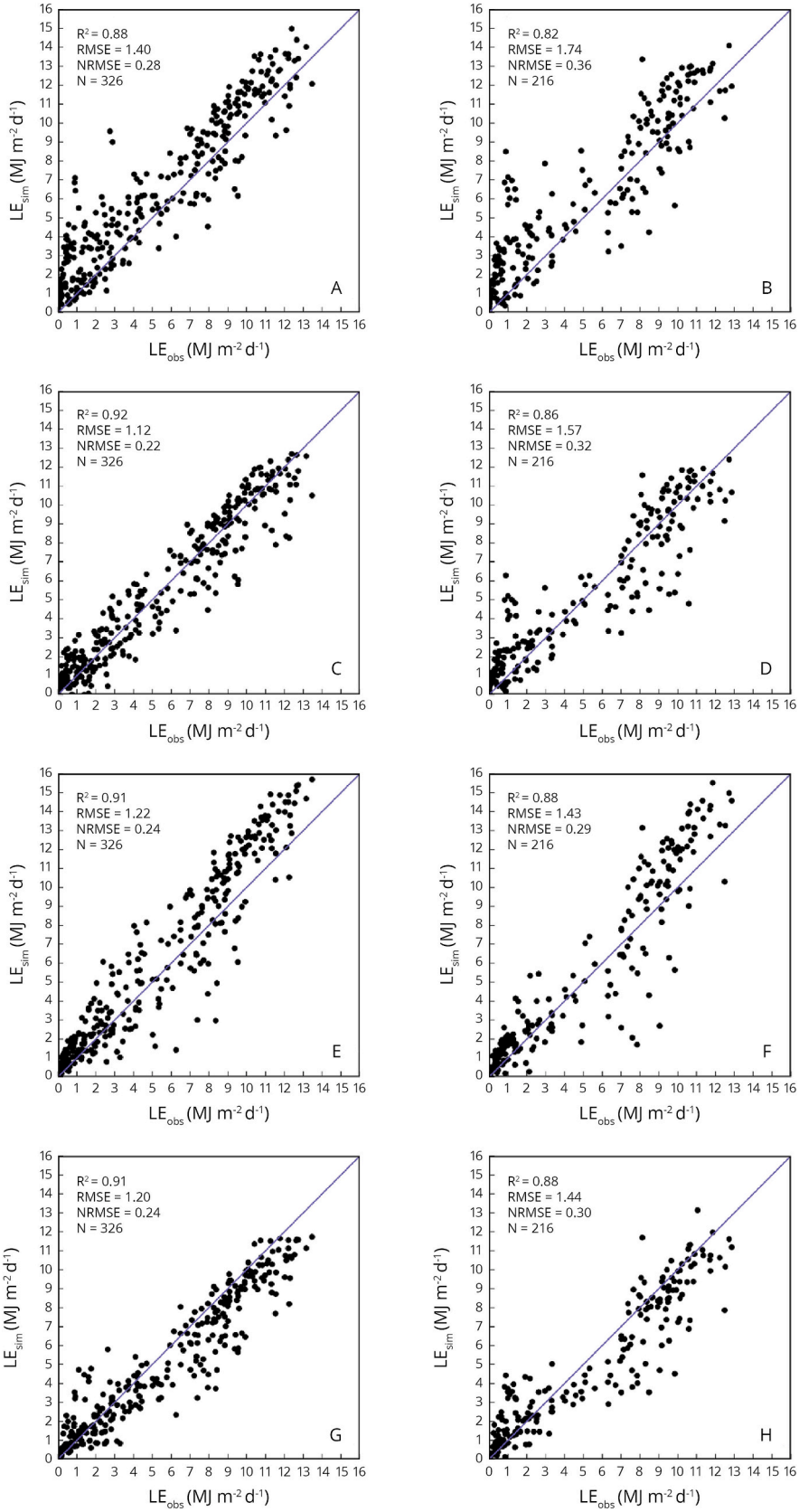

Fig. 4. Performance of PT-JPL ET expressed in energy terms (latent heat, LE) on the Kapiti calibration (left) and validation (right) EC flux and FloX subsets for the original PT-JPL (A-B), HVI ET_C with the original PT-JPL ET_S (C-D), original PT-JPL ET_C with HVI ET_S (*E*-F), and HVI ET_C and ET_S combined (G-H).

hyperspectral narrowbands. Across configurations, improvements were most pronounced in the reduction of systematic bias rather than large gains in correlation, underscoring the role of hyperspectral information in correcting structural error within PT-JPL.

Fig. 5 shows the daily dynamics of observed and simulated ET across the two study periods: 2019–2020 and 2023–2024. Both time series exhibit two distinct ET peaks that align with the onset of the long and short rains. In drylands such as Kapiti, the onset of the rains rapidly recharges soil moisture, reactivates vegetation, and drives sharp increases in ET. Between these peaks, soil moisture declines quickly and dry-season conditions prevail, resulting in lower ET. The 2019–2020 period experienced flooding, with an extended rainy season that produced higher and more sustained ET values. During this period, the original PT-JPL aligned well with observed ET, while the HVI ET_C and combined ($ET_C + ET_S$) PT-JPL versions tended to slightly underestimate ET. This modest underestimation may reflect transient surface water or waterlogged soil conditions on the Vertisol-dominated footprint, which can enhance evaporation beyond what is represented in PT-JPL ET_S, as the model does not explicitly account for open-water evaporation. The HVI ET_S configuration also underestimated ET during this period, consistent with the dry down between the long and short rains. In contrast, the 2023–2024 period coincided with an El Niño event that brought above-average rainfall to Kenya. Under these conditions, larger discrepancies among model variants emerged. The original PT-JPL and HVI ET_S versions clearly overestimated ET during the short rains, whereas the HVI ET_C produced the closest agreement with observations, both individually and when combined with HVI ET_S. The ET_S overestimation is consistent with the inflation mechanism described earlier, whereby elevated humidity and atmospheric demand increase PET, while surface soil moisture supply remains limiting. In such cases, the RH/VPD-based soil moisture constraint in the original PT-JPL fails to fully suppress soil evaporation, resulting in positive ET bias. Overall, The optimized HVIs reduced this inflation and improved temporal correspondence, particularly under El Niño conditions.

4.2. Optimized PT-JPL ET and ESI over Kapiti and surrounding areas

Figs. 6 and 7 show ET and ESI estimated with EnMAP and PRISMA for 18 March 2023. The artifacts reflect the coarse (0.1°) AgERA forcing, which introduces block-like discontinuities at 30 m resolution. This may affect absolute ET magnitude, but it does not influence the comparative assessment, as identical forcing was applied across all model configurations. For both sensors, ET values were generally low (0–7 MJ m^{-2} d^{-1}) during the late dry-season brown-down period, reflecting drought-induced dormancy rather than active growth. The corresponding EnMAP and PRISMA results for 23 February 2023 are provided in the Supplement (Figs. S3 and S4) and mirror the results presented here. ET was relatively high over the central ridge of Kapiti and Kyamutheke Hill in the northeast. These areas are dominated by woody vegetation with deeper water access. The AusQuest farm also showed elevated ET, reflecting crop development. Low ET values on the northern and southeastern edges of the images correspond to built-up village and science park infrastructure, respectively. No land-cover mask was applied; however, these pixels generally exhibited low ET due to minimal vegetation cover and low soil evaporation. ET derived from the original PT-JPL tended to be higher than that estimated from the HVI-driven versions, which is consistent with the bias observed in the scatterplots and time series plots. This overestimation is most apparent along the ridge, Kyamutheke Hill, and built-up areas, which represent the upper and lower bounds of ET in the images. Residual bias in the built-up areas likely reflects simplified surface assumptions rather than active transpiration processes. Overestimation of the original PT-JPL ET leads to overestimates of ESI as well. Because drought likelihood increases as ESI declines, the overestimation signals an increased likelihood of Type II errors (i.e., missed drought detections).

4.3. Evaluation of optimized PT-JPL ET and ESI over AusQuest farm

The relationships between simulated and observed ET at the AusQuest EC flux tower were weaker than those at Kapiti, with R^2 values lower by half (Fig. 8). Errors, however, were smaller, reflecting the limited sample size and narrower dynamic range of the validation data. A clear positive bias was evident in the original PT-JPL simulations with EnMAP and PRISMA NDVIs. This bias was substantially reduced in the PT-JPL simulations driven by EnMAP HVIs and to a lesser extent by PRISMA HVIs. Overall, the HVI-based PT-JPL versions performed considerably better than the original model, with R^2 increasing by 0.09 and 0.12 and RMSE decreasing by 0.07 and 0.06 MJ m^{-2} d^{-1} for EnMAP and PRISMA, respectively.

5. Discussion

Our study set out to address a key limitation of PT-JPL: its systematic overestimation of ET in dryland ecosystems caused by weak partitioning. We approached this by parameterizing the mission-standard ECOSTRESS PT-JPL product with HVIs, which Marshall et al. (2016) showed can improve partitioning, thereby reducing ET estimation errors considerably. Our findings, illustrated in Fig. 5, demonstrate that HVI-driven ECOSTRESS PT-JPL reduced the positive ET bias in the standard NDVI and RH/VPD configuration observed by Hu et al. (2023a) and Liang et al. (2022). This reduction in ET bias translated into lower ESI values under moisture-limited conditions, which is expected to reduce omission risk in ET-based drought monitoring, however independent impact data would be needed to confirm. Improvements were consistent across multiple hydrological years, sensor platforms, and validation datasets, underscoring the robustness of hyperspectral information in constraining canopy and soil evaporation processes in moisture-limited environments. These results reinforce a broader point raised in the introduction: as aridity intensification continues to decouple precipitation and ET in many of the world's drylands, ET-based drought indicators will depend on accurate representation of vegetation biochemical and biophysical dynamics (Zhou et al., 2019; Lian et al., 2021). Hyperspectral imaging, especially when combined with thermal observations from ECOSTRESS and forthcoming missions such as LSTM, offers a clear pathway toward meeting this need. The subsections that follow examine these findings in detail, focusing on (i) HNB-driven improvements in PT-JPL performance; (ii) model behavior across contrasting hydrological years; (iii) spatial performance and implications for drought early-warning; (iv) scalability and transferability of the proposed approach; and (v) suggestions for future missions: hyperspectral–thermal–microwave synergy.

5.1. HNB-driven improvements in PT-JPL performance

The optimization of PT-JPL with HVIs improved ET estimates at Kapiti, although not to the same degree reported by Marshall et al. (2016). Much of this difference can be attributed to the way ET was partitioned and analysed in the two studies. In Marshall et al. (2016), ET_C and ET_S were partitioned with F_{IPAR} derived from LAI measured with a handheld ceptometer. The ceptometer provided above- and below-canopy shortwave radiation measurements from which LAI was retrieved. HVIs were then statistically related to ET_C and ET_S. In contrast, our study partitioned ET with both F_{IPAR} and F_{APAR} derived from hyperspectral reflectance, after which simulated PT-JPL ET_C and ET_S were statistically related to observed ET. The heavier reliance on modelled ET components in our study naturally led to lower correlations than when HVIs were related directly to physically partitioned flux components.

Another difference concerns the spectral regions identified as most important. Marshall et al. (2016) found that the highest-performing HVIs were essentially hyperspectral NDVIs with pairings dominated by red and NIR HNBs. In our study, HNBs in the visible green region were

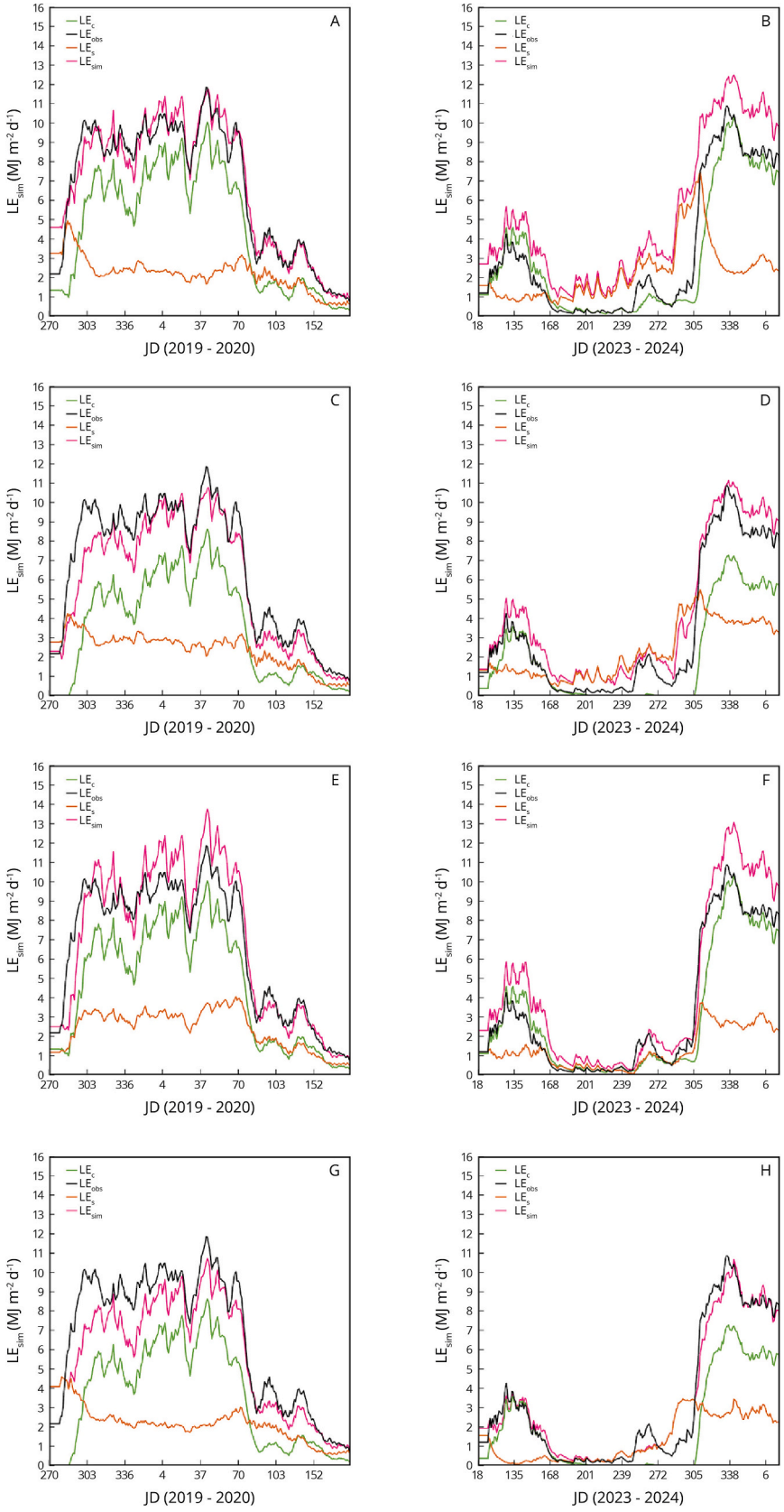

Fig. 5. Julian day (JD) ime series of observed (obs) and simulated (sim) PT-JPL ET expressed in energy terms (latent heat, LE) during the 2019–2020 (left) and 2023–2024 (right) periods for the original PT-JPL (A-B), HVI ET_C with the original PT-JPL ET_S (C-D), original PT-JPL ET_C with HVI ET_S (E-F), and HVI ET_C and ET_S (G-H). The time series are decomposed into the simulated canopy (LE_C) and soil (LE_S) components.

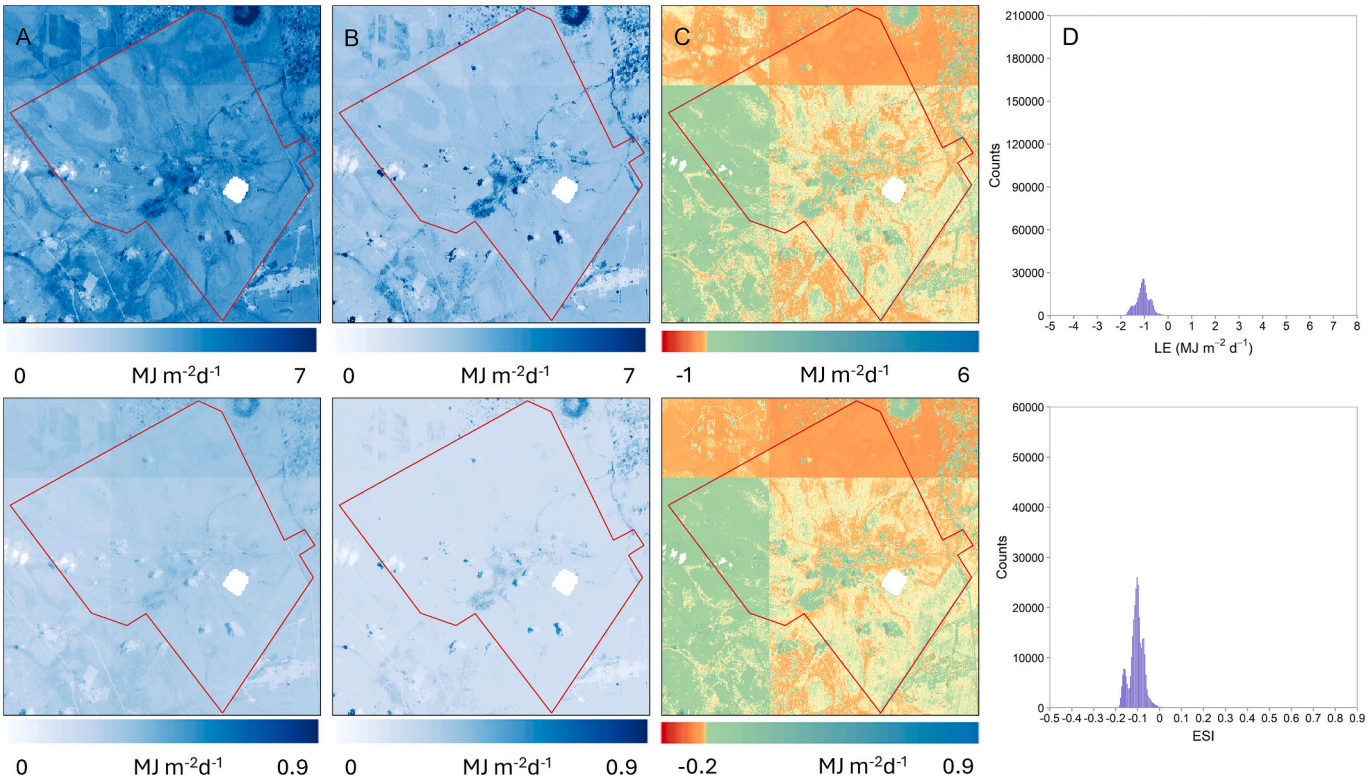

Fig. 6. Spatial distribution of ET and ESI over Kapiti and surrounding areas as estimated by EnMAP NDVI and HVIs on 18 March 2023. The upper (ET) and lower (ESI) panels show estimates from the original PT-JPL (A), HVI-driven PT-JPL (B), difference between the two (HVI-driven PT-JPL – original PT-JPL) (C), and histogram of differences for all pixels (D). ET and ESI are displayed using a sequential color scale, while difference maps use a diverging color scale.

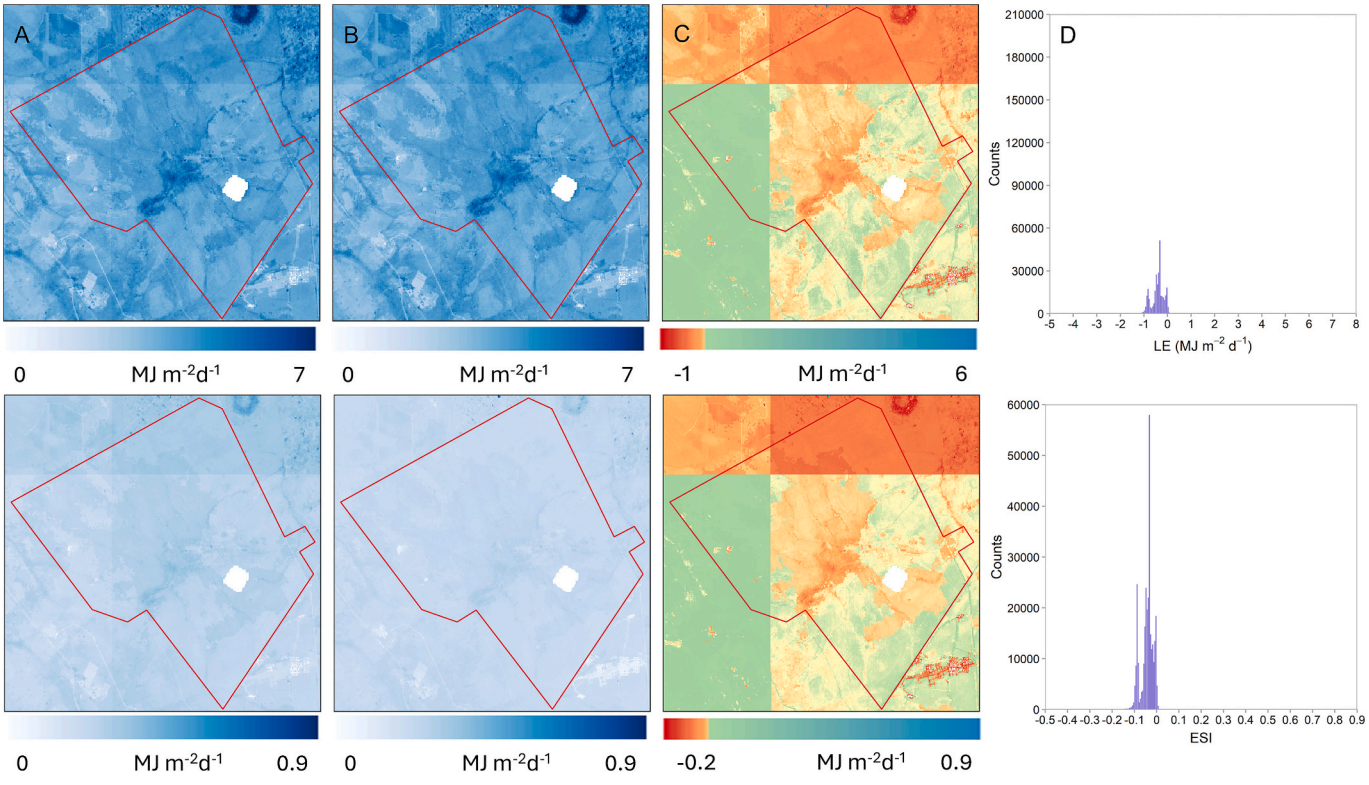

Fig. 7. Spatial distribution of ET and ESI over Kapiti and surrounding areas as estimated by PRISMA NDVI and HVIs on 18 March 2023. The upper (ET) and lower (ESI) panels show estimates from the original PT-JPL (A), HVI-driven PT-JPL (B), difference between the two (HVI-driven PT-JPL – original PT-JPL) (C), and histogram of differences for all pixels (D). ET and ESI are displayed using a sequential color scale, while difference maps use a diverging color scale.

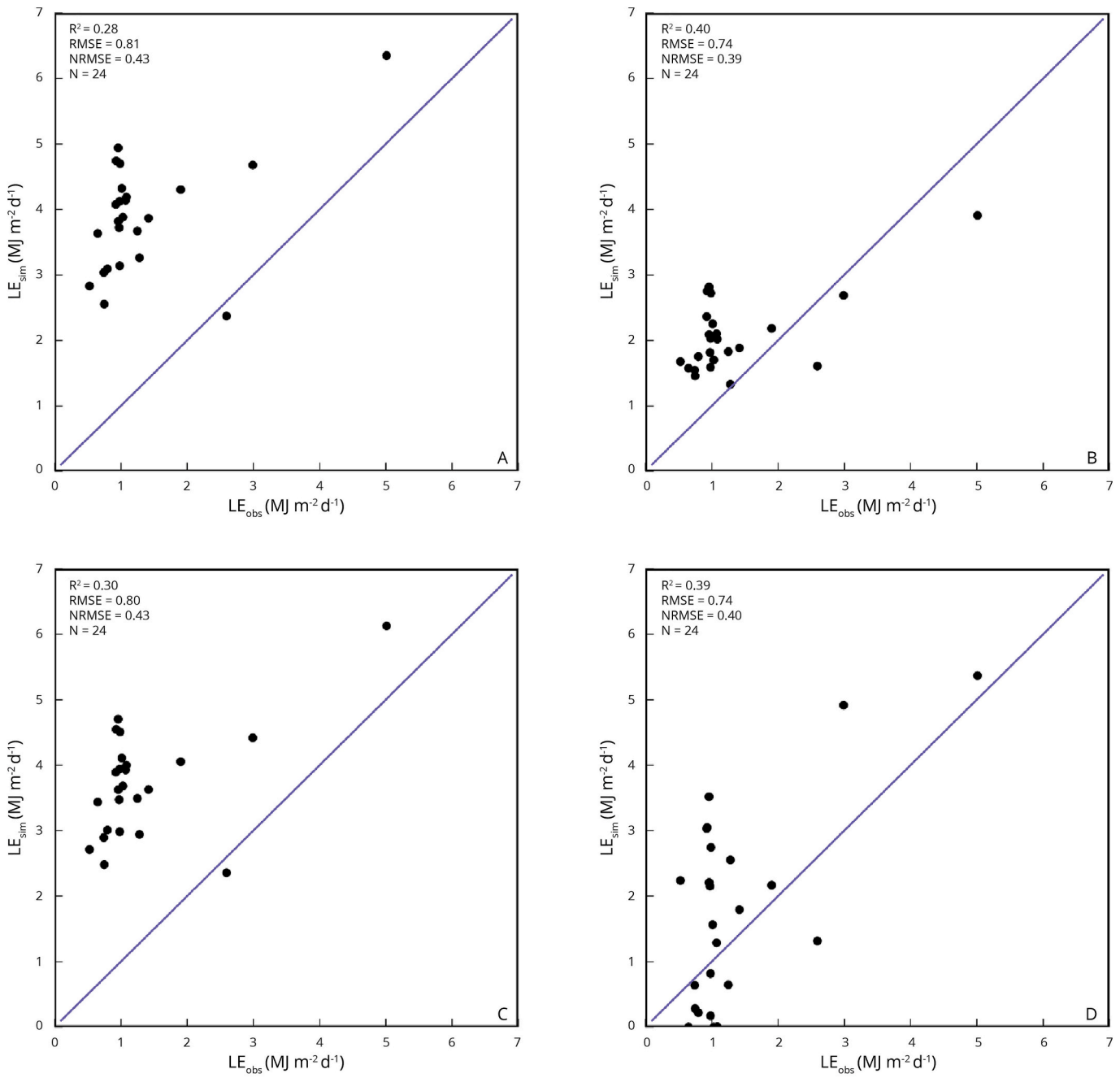

Fig. 8. Performance of PT-JPL ET expressed in energy terms (latent heat, LE) for the AusQuest farm EC flux data with EnMAP and PRISMA NDVI (A&C) and HVIs (B&D).

more influential. This region is sensitive to chlorophyll concentration and photosynthetic pigment dynamics, and our partitioning explicitly accounts for absorption of PAR by the photosynthetically active ("green") portion of the canopy via F_{APAR}. Recent work using high-resolution thermal imaging at the individual-tree scale further demonstrates that transpiration responses to drought vary strongly with canopy physiology and species composition (Javadian et al., 2024), reinforcing the need for physiologically sensitive spectral constraints in ET models.

The performance of ET_S in our study also contrasts with Marshall et al. (2016), where transpiration dominated ET variability in irrigated croplands and soil evaporation contributed comparatively little. In PT-JPL, ET_S often accounts for a smaller fraction of total ET (typically <40%) and is therefore frequently treated as a secondary term. However, at Kapiti, ET_S emerged as a comparatively strong source of variability. This is particularly important because soil evaporation is the principal structural weakness of PT-JPL in drylands, where its dependence on near-surface humidity can inflate ET under moisture-limited conditions (Marshall et al., 2020; Purdy et al., 2018). The contrasting hydrologic context likely explains this shift: whereas the Central Valley study examined persistently irrigated systems with sustained transpiration, Kapiti is characterized by extended dry periods punctuated by rainfall events, during which exposed soil and shallow moisture pulses drive rapid but transient evaporation. Under these conditions, hyperspectral sensitivity to soil moisture, non-photosynthetic vegetation, and exposed soil background becomes particularly valuable. A limitation of our study is the spectral range of the FloX tower. Even though the instrument provided high-frequency hyperspectral measurements

uniquely suited for ET model optimization, it detected only from 400 to 950 nm. In Marshall et al. (2016), the best-performing ET_S HVIs included NIR combinations centred on 953 nm, which is just beyond the range of FloX. This region coincides with a water absorption feature that the authors speculated may help normalize differences in HNB combinations. Studies, including Marshall et al. (2020) and Zhang et al. (2021), have since emphasized the relevance of longer-wavelength water absorption features in the SWIR for constraining ET_S. New autonomous field spectrometers with SWIR coverage (up to ~1500-1700 nm with a FWHM of 10 nm) are now available, geographically distributed, and with open access through hyperspectral networks such as HYPERNETS (Ruddick et al., 2024). Coupled with longer time series of EnMAP and PRISMA data, these instruments offer an opportunity to evaluate whether SWIR HVIs can further enhance ECOSTRESS PT-JPL ET_S in dryland environments.

5.2. Model behavior across contrasting hydrological years

Model performance differed noticeably across the two hydrological regimes of 2019–2020 and 2023–2024 (Fig. 6). The 2019–2020 period was complex: the short rains of 2019 were exceptionally wet and produced widespread flooding, whereas the long rains of 2020 were closer to normal, followed by a progressive dry-down that triggered the Horn of Africa drought. In contrast, 2023–2024 was characterized by consistently above-average rainfall across much of Kenya due to El Niño, resulting in more stable soil moisture availability and vegetation activity throughout the period. We acknowledge that energy balance closure using the Bowen ratio method may introduce additional uncertainty during wet or near-saturated conditions when sensible heat flux approaches zero, potentially contributing to some of the observed discrepancies. These conditions are most likely to occur during the 2019–2020 wet period, and may contribute to the observed discrepancies between modelled and observed ET during this time.

ET models generally perform better during sustained wet periods than during episodes in which rainfall, soil moisture, and vegetation activity fluctuate rapidly (Hu et al., 2023). This pattern was evident in our results. During the hydrologically complex 2019–2020 sequence, the HNB-driven PT-JPL configurations tended to underestimate ET, while the original PT-JPL performed comparatively better. One likely explanation is that our optimization was based on a subset stratified by high and low ET values across both study periods. Although broadly representative, this approach may have produced more conservative estimates of ET_S during intense wet pulses and reduced sensitivity to residual soil evaporation during extended dry-downs, leading to slight underestimation when conditions shifted rapidly between wet and dry states.

In contrast, the behavior of the models reversed during the 2023–2024 El Niño period. The original PT-JPL clearly overestimated ET, while the HVI-based configuration provided the closest agreement with observed ET. During 2023–2024, RH was consistently higher and VPD lower, which PT-JPL interprets as a steady supply of soil moisture via F_{SM}. Between rainy seasons, this produced modest positive ET biases because atmospheric humidity remained elevated longer than surface moisture. However, at the peaks of the rainy seasons, the bias mechanism shifted. Under moist conditions, F_{SM} approaches one, effectively removing the moisture limitation on ET_S. With F_{SM} near unity and abundant net radiation, PT-JPL drives ET_S toward its potential rate, even when the surface cannot supply water at that rate. The HVI-based configuration avoided this behavior not by modifying ET_S directly, but by providing a more realistic constraint on canopy transpiration. Because PT-JPL partitions total available energy between ET_C and ET_S, a more physiologically grounded HVI-based ET_C tightened the overall energy balance thereby dampening the inflation of ET_S under humid El Niño conditions.

Although our two study periods captured contrasting hydrological regimes, the data gap between them unfortunately coincided with the heart of the Horn of Africa drought. As longer, continuous multi-year time series of ET become available, future studies should examine how hyperspectral constraints perform across the spectrum of dryland hydrological variability, including extreme drought conditions. Such analyses will be essential for advancing ET-based drought indicators and strengthening their integration into operational early-warning systems.

5.3. Spatial performance and implications for drought early-warning

The spatial analysis corroborated the temporal results and highlighted where PT-JPL's structural limitations are most apparent across the landscape. ET was consistently higher in areas with denser woody vegetation and access to deeper soil moisture, while sparsely vegetated and more rainfall-dependent areas exhibited lower ET (Figs. 7 and 8). Across these gradients, the original PT-JPL systematically overestimated ET at both the lower and upper ends of the moisture spectrum, but for different reasons. At the dry end, the positive bias was driven by the ET_S dependence on RH/VPD, which elevates the soil-evaporation constraint even when the soil surface is moisture-limited. At the wet end, however, the bias stemmed from a different mechanism. NDVI saturation at high canopy density causes the f_{APAR}-based transpiration constraint in PT-JPL to approach unity prematurely. When f_{APAR} saturates, further increases in canopy structure are not represented, allowing both ET_C and ET_S to expand toward potential rates and weakening the model's ability to correctly partition available energy, thereby inflating total ET. This behavior was newly documented in our analysis. The hyperspectral configuration mitigated both sources of bias. HVIs provided a stronger biochemical and biophysical constraint on ET_C. At the same time, their sensitivity to vegetation moisture, structure, and pigment dynamics improved the estimation of F_{SM} across the drier parts of the landscape, preventing ET_S from dominating the ET signal. The combined effect was a noticeably lower bias in ESI across the full range of moisture conditions. These improvements were consistent across two phenologically distinct dates for both EnMAP and PRISMA, despite differences in sensor characteristics, providing a positive outlook for forthcoming hyperspectral missions with similar spectral configurations and operational acquisition strategies (e.g., CHIME, SBG).

An important challenge in the spatial interpretation concerns scale mismatches between observations and model inputs. Ground-based hyperspectral reflectance represents a footprint of ~1–2 m and eddy covariance fluxes integrate over hundreds of meters, while 30 m satellite data were combined with meteorological forcing at ~10 km resolution for spatial extension. This approach assumes that relationships calibrated at the plot scale can be transferred across scales and applied with satellite and reanalysis data. This assumption is reasonable for the relatively homogeneous Kapiti site, but may introduce uncertainty in the absolute magnitude of ET, particularly under dynamically varying atmospheric conditions such as the El Niño period considered here. At the same time, spatial variability in ET at the field scale is expected to be primarily vegetation-driven, which helps preserve relative spatial patterns despite the coarse meteorological forcing. Because identical forcing was applied across all model configurations, the comparative improvements associated with hyperspectral constraints remain robust. Nevertheless, future applications would benefit from image-scale calibration as more frequent hyperspectral observations become available, as well as from higher-resolution meteorological forcing to reduce these uncertainties in more heterogeneous landscapes.

FEWS NET and national agencies such as Kenya's National Drought Management Authortiy primarily rely on rainfall anomalies and vegetation indicators (e.g., NDVI), and increasingly incorporate ET-based products such as SSEBop and MOD16. However, these broadband ET products are subject to many of the same structural and partitioning biases identified here. A central operational priority for these early-warning systems is to minimize omission errors (i.e., missed drought events) because the consequences of delayed response far outweigh those of false alarms. Although our analysis was limited to a relatively

small study area, two hydrological periods, and two pairs of hyperspectral satellite acquisitions, the results demonstrate that omission errors can be reduced when HVIs are incorporated into drought-monitoring workflows. Reliable ET estimates are essential as droughts evolve from negative precipitation anomalies to soil-moisture deficits (Choi et al., 2013), during rapidly developing "flash" droughts where vegetation stress emerges before rainfall declines (Otkin et al., 2014), and in near-normal rainy years when ET is suppressed by aridity intensification (Zhou et al., 2019). By reducing bias in both ET and ESI across heterogeneous dryland landscapes, hyperspectral constraints offer the potential for earlier and more spatially consistent identification of emerging water stress. This has direct implications for decision-makers: improved ET-based indicators enable agencies to provide more timely advisories to farmers and pastoralists, support more accurate triggers for crop and livestock insurance payouts, and otherwise more effectively target resources to prevent crop failure, livestock losses, and distressed sales.

5.4. Scalability and transferability of the HVI-based PT-JPL framework

It is important to consider the transferability of the proposed approach given that it is demonstrated here at a single experimental site. The framework is grounded in physically meaningful relationships between hyperspectral reflectance and biophysical surface properties. Within PT-JPL, ET is regulated through multiplicative constraint functions governing ET_C and ET_S. By replacing broadband NDVI- and RH/VPD-based parameterizations with HVIs that are sensitive to chlorophyll content, pigment dynamics, canopy structure, and surface moisture conditions, the modifications introduced here strengthen the physical representation of these constraints rather than relying on purely empirical or site-specific calibration. Because these spectral–biophysical relationships are general, the approach is expected to be transferable across moisture-limited ecosystems where ET variability is primarily controlled by vegetation condition and soil moisture availability.

Practical considerations remain important for broader application. These include the need for regional calibration of HVI formulations to account for differences in vegetation composition and soil background, the influence of meteorological forcing resolution on absolute ET magnitude, and the availability and consistency of hyperspectral observations. The multiplicative structure of PT-JPL further enables improvements in individual constraint terms to propagate directly to total ET and its partitioning, providing a scalable pathway for enhancing ET estimation. This behavior contrasts with more internally constrained frameworks such as the TSEB model, where tighter coupling between model components can dampen the impact of improved input variables, resulting in smaller gains in ET partitioning when incorporating hyperspectral information (Richter and Timmermans, 2009).

5.5. Implications for future missions: hyperspectral–thermal–microwave synergy

Recent efforts to improve ET estimation in drylands have explored a range of remote sensing constraints, including broadband vegetation indices, thermal infrared observations, microwave soil moisture retrievals, and solar-induced chlorophyll fluorescence. Broadband indices such as NDVI and EVI are widely used but are limited by saturation at high canopy density and reduced sensitivity to physiological stress. Thermal approaches provide strong constraints on surface energy balance but do not directly resolve vegetation biochemical or structural dynamics. Microwave observations offer valuable information on soil moisture but at coarse spatial resolution, limiting their applicability for field-scale drought monitoring. Fluorescence-based approaches provide direct links to photosynthesis but remain constrained by signal availability and spatial resolution. In contrast, hyperspectral observations provide contiguous narrowband information that captures subtle variations in canopy biochemistry, structure, and moisture status. This enables improved representation of both canopy transpiration and soil evaporation processes within ET models. The results presented here demonstrate that hyperspectral constraints complement existing thermal and microwave observations by addressing key structural limitations of broadband approaches, particularly NDVI saturation and soil evaporation inflation in dryland environments.

A key limitation of our study is its restricted spatial and temporal coverage, which emphasizes the need for next-generation hyperspectral, thermal, and microwave missions. These complementary capabilities are reflected in upcoming satellite systems. LSTM will provide routine diurnal LST observations with the accuracy needed for energy-balance ET models (Zhang et al., 2025) while Landsat NeXt, S2NG, CHIME, and SBG will supply frequent VIS–NIR–SWIR reflectance with new red-edge and SWIR narrowbands relevant for constraining both ET_C and ET_S. CHIME and SBG will further deliver continuous 400–2500 nm hyperspectral coverage, enabling retrievals of canopy biochemistry, non-photosynthetic vegetation, and soil properties that directly influence ET partitioning.

L-band microwave missions such as ROSE-L and ongoing SMAP observations provide all-weather soil-moisture constraints that complement the optical–thermal domain (Purdy et al., 2018). Together, these multi-sensor data streams can be integrated into PT-JPL, ALEXI, and TSEB frameworks, paving the way for more accurate ET, improved ESI, and stronger drought early-warning capacity in dryland regions. Although hyperspectral processing is more computationally intensive than broadband NDVI workflows, operational feasibility is increasing with cloud-based platforms, preprocessed Level-2 reflectance products, and the limited number of narrowband ratios required for ET partitioning. The approach demonstrated here relies on a small set of optimized band combinations rather than full spectral inversion, reducing computational burden and making integration into national drought workflows increasingly realistic.

6. Conclusion

Evapotranspiration (ET) is a critical indicator of drought development in Africa's drylands and forms the basis of emerging operational early-warning systems. While ET can be estimated from biophysical parameters derived from Earth Observation, its accuracy remains limited in moisture-constrained environments where vegetation and soil processes respond rapidly to atmospheric forcing. In PT-JPL, soil evaporation is particularly challenging because its constraint relies heavily on near-surface humidity, which can become decoupled from actual soil moisture under dryland conditions. In this study, hyperspectral narrowbands from field spectrometry, EnMAP, and PRISMA reduced this structural limitation by strengthening constraints on both canopy transpiration and soil evaporation. On the independent validation subset, the standard PT-JPL overestimated ET by 21.8%, whereas hyperspectral parameterizations reduced bias to 3.5% and − 6.4% depending on configuration, while also improving R^2 and RMSE. These improvements were most pronounced under humid and transitional conditions, where the original parameterization inflated soil evaporation. Together, these findings demonstrate that narrowband spectral information captures biochemical and biophysical controls on ET partitioning that broadband indices cannot resolve, thereby directly reducing structural bias in PT-JPL under moisture-limited conditions. While our analysis was limited in spatial and temporal extent, the results indicate that integrating hyperspectral constraints into ET models can reduce systematic bias and improve the physical consistency of ET-based drought indicators. Upcoming missions—including Landsat NeXt, Sentinel-2 Next Generation, CHIME, and SBG—combined with thermal and microwave observations, provide a feasible pathway toward operational implementation and stronger drought early-warning capacity in climate-vulnerable drylands.

Supplementary data to this article can be found online at https://doi.org/10.1016/j.rse.2026.115453.

CRediT authorship contribution statement

Michael Marshall: Writing – review & editing, Writing – original draft, Visualization, Validation, Supervision, Software, Resources, Project administration, Methodology, Investigation, Funding acquisition, Formal analysis, Data curation, Conceptualization. **Monica Pepe:** Writing – review & editing, Visualization, Validation, Supervision, Software, Resources, Project administration, Methodology, Investigation, Formal analysis, Data curation, Conceptualization. **Giulia Tagliabue:** Writing – review & editing, Visualization, Validation, Software, Resources, Methodology, Investigation, Formal analysis, Data curation, Conceptualization. **Vincent Odongo:** Writing – review & editing, Resources, Methodology, Investigation, Formal analysis, Data curation, Conceptualization. **Wim Timmermans:** Writing – review & editing, Validation, Software, Resources, Project administration, Methodology, Investigation, Formal analysis, Data curation, Conceptualization. **Francesco Vuolo:** Writing – review & editing, Validation, Methodology, Investigation, Formal analysis, Data curation. **Agnieszka Soszynska:** Writing – review & editing, Software, Resources, Methodology, Investigation, Formal analysis, Data curation, Conceptualization. **Kwasi Ofori-Karikari:** Writing – review & editing, Software, Methodology, Investigation, Data curation. **Egor Prikaziuk:** Writing – review & editing, Visualization, Methodology, Investigation, Formal analysis, Conceptualization. **Volkan Yilmaz:** Writing – review & editing, Visualization, Methodology, Investigation, Formal analysis, Data curation. **Serkan Girgin:** Visualization, Software, Resources, Methodology, Investigation, Data curation. **Cinzia Panigada:** Writing – review & editing, Software, Methodology, Investigation, Data curation, Conceptualization. **Micol Rossini:** Writing – review & editing, Methodology, Investigation, Conceptualization. **Francesco Fava:** Writing – review & editing, Supervision, Resources, Methodology, Investigation, Conceptualization. **Sonja M. Leitner:** Writing – review & editing, Supervision, Resources, Methodology, Investigation, Conceptualization. **Christoph Hecker:** Writing – review & editing, Supervision, Methodology, Investigation, Data curation, Conceptualization. **Lutz Merbold:** Writing – review & editing, Resources. **Zoltan Szantoi:** Supervision, Resources, Conceptualization. **Mirco Boschetti:** Writing – review & editing, Validation, Methodology, Investigation, Formal analysis, Data curation, Conceptualization.

Declaration of competing interest

The authors declare that they have no known competing financial interests or personal relationships that could have appeared to influence the work reported in this paper.

Acknowledgments

Our research was primarily supported by the European Space Agency (ESA) EO AFRICA – EXPLORERS EXPRO+EO funding mechanism under ESA Contract 4000133905/21/I-EF and titled, "HyRELIEF: Enhancing ECOSTRESS drought monitoring with hyperspectral narrowbands" (https://www.itc.nl/hyrelief/). The authors would like to further acknowledge the PRISCAV project (ASI Contract 2019–5-HH-0) for supporting the framework used to assess PRISMA data quality and to configure image pre-processing. Vincent Odongo and Sonja M. Leitner acknowledge funding from the CGIAR Trust Fund received through the Science Programs Multifunctional Landscapes and Climate Action. CGIAR is a global research partnership for a food-secure future dedicated to transforming food, land, and water systems in a climate crisis. Furthermore, the authors would like to thank the team of the Kapiti Research Station & Wildlife Conservancy, particularly Ilona Gluecks, Nehemiah Kimengich, Nelson Kipchirchir, and Sospeter Wambugu, for their support in maintaining the Eddy Covariance flux tower and providing Kapiti data. We also recognize the National Drought Management Authority and the Regional Centre for Mapping of Resources for Development in Nairobi, Kenya, whose collaboration helped clarify user needs and system requirements for drought monitoring. Their contributions were instrumental in co-developing the HVI-adapted ECOSTRESS workflow presented in this study. Finally, to Dr. Clement Atzberger at dClimate Labs for his role in project conceptualization, and to Dr. Josh Fisher at Chapman University for his expert guidance on the ECOSTRESS PT-JPL model framework.

Data availability•

In-situ data: Eddy covariance (EC) flux measurements and hyperspectral reflectance data collected at the Kapiti Research Station & Wildlife Conservancy and the AusQuest farm (Kenya) were used for model calibration and validation. These datasets include latent and sensible heat fluxes, meteorological variables, and canopy reflectance acquired with a FloX field spectrometer. Due to third-party ownership and site-specific data-sharing agreements, raw in-situ datasets cannot be made fully publicly available. Processed datasets, including daily aggregated fluxes and quality-controlled reflectance spectra used in this study, will be archived upon publication on Zenodo (doi:https://doi.org/10.5281/zenodo.XXXXXXX). Access to raw data may be granted upon reasonable request and subject to approval by the data providers.•

Satellite and ancillary data: All satellite and ancillary datasets used in this study are publicly available or accessible through standard data portals. ECOSTRESS land surface temperature (LST), emissivity, and precipitable water vapor (PWV) were obtained via the NASA AppEEARS platform. Hyperspectral imagery from EnMAP and PRISMA was acquired through mission tasking, subject to mission-specific data policies. Landsat-8 surface reflectance data were obtained from the USGS EarthExplorer portal, Sentinel-2 data from ESA Copernicus services, and aerosol optical properties from the MODIS MOD04 product. Agrometeorological variables were derived from the AgERA5 dataset, and additional contextual data from the FAO WaPOR database.•

Derived data products: This study generated spatial ET estimates, including partitioned canopy transpiration (ET_C) and soil evaporation (ET_S), as well as evaporative stress index (ESI) maps and hyperspectral vegetation indices (HVIs). These derived datasets are provided as cloud-optimized GeoTIFFs via a STAC catalog (https://data.crib.utwente.nl/stac/hyrelief/catalog.json) and will be archived on Zenodo (doi: https://doi.org/10.5281/zenodo.XXXXXXX).•

Code availability: Code used for data processing, PT-JPL model implementation, hyperspectral index optimization, and figure generation was developed in R and Python. The code is publicly available via a GitHub repository (https://github.com/xxx/yyy) and will be archived on Zenodo (doi:https://doi.org/10.5281/zenodo.XXXXXXX) to support transparency and reuse. Some preprocessing steps rely on external tools and workflows (e.g., atmospheric correction and co-registration), and full end-to-end reproducibility may require additional configuration.

References

Anderson, M.C., Norman, J.M., Mecikalski, J.R., Otkin, J.A., Kustas, W.P., 2007. A climatological study of evapotranspiration and moisture stress across the continental United States based on thermal remote sensing: 1. model formulation. J. Geophys. Res. Atmos. 112. https://doi.org/10.1029/2006JD007506.

Anderson, M.C., Kustas, W.P., Norman, J.M., Hain, C.R., Mecikalski, J.R., Schultz, L., González-Dugo, M.P., Cammalleri, C., d'Urso, G., Pimstein, A., Gao, F., 2011. Mapping daily evapotranspiration at field to continental scales using geostationary and polar orbiting satellite imagery. Hydrol. Earth Syst. Sci. 15, 223–239. https://doi.org/10.5194/hess-15-223-2011.

Andres-Anaya, P., Sanchez-Aparicio, M., Del Pozo, S., Lagüela, S., Hernández-López, D., Gonzalez-Aguilera, D., 2024. A new methodology for estimating surface albedo in heterogeneous areas from satellite imagery. Appl. Sci. 14, 75. https://doi.org/10.3390/app14010075.

Bernard, F., Manolis, I., Barat, I., Alamañac, A.B., Taboada, M.S., Mingorance, P., Ciapponi, A., Cardone, T., Nunez, I.F., Garcia, A., Hallibert, P., Hammar, A., Henriot, P., Codinachs, D.M., Patti, S., Montes, P.P., Skrzypek, P., Steenari, D., Weixler, S., Deslous, S., Coatantiec, C., Trotta, O.A., Vega, I.C., Holgueras, D.G., 2023. The copernicus land surface temperature monitoring (LSTM) mission: design,

technology and status. In: Sensors, Systems, and Next-generation Satellites XXVII. Presented at the Sensors, Systems, and Next-generation Satellites XXVII, SPIE, pp. 41–55. https://doi.org/10.1117/12.2679705.
Bouchet, R., 1963. Evapotranspiration reelle at potentielle, signification climatique. In: Int Assoc Sci Hydro Pub, 62, pp. 134–142.
Campbell, G.S., Norman, J.M., 1998. An Introduction to Environmental Biophysics, 2nd ed. Springer, New York, NY.
Choi, M., Jacobs, J.M., Anderson, M.C., Bosch, D.D., 2013. Evaluation of drought indices via remotely sensed data with hydrological variables. J. Hydrol. 476, 265–273. https://doi.org/10.1016/j.jhydrol.2012.10.042.
Elzhov, T.V., Mullen, K.M., Spiess, A.N., Bolker, B., 2015. Package 'minpack.lm.'.
Ershadi, A., McCabe, M.F., Evans, J.P., Chaney, N.W., Wood, E.F., 2014. Multi-site evaluation of terrestrial evaporation models using FLUXNET data. Agric. For. Meteorol. 187, 46–61. https://doi.org/10.1016/j.agrformet.2013.11.008.
Fisher, J.B., Tu, K.P., Baldocchi, D.D., 2008. Global estimates of the land–atmosphere water flux based on monthly AVHRR and ISLSCP-II data, validated at 16 FLUXNET sites. Remote Sens. Environ. 112, 901–919. https://doi.org/10.1016/j.rse.2007.06.025.
Fisher, J.B., Melton, F., Middleton, E., Hain, C., Anderson, M., Allen, R., McCabe, M.F., Hook, S., Baldocchi, D., Townsend, P.A., Kilic, A., Tu, K., Miralles, D.D., Perret, J., Lagouarde, J.-P., Waliser, D., Purdy, A.J., French, A., Schimel, D., Famiglietti, J.S., Stephens, G., Wood, E.F., 2017. The future of evapotranspiration: global requirements for ecosystem functioning, carbon and climate feedbacks, agricultural management, and water resources. Water Resour. Res. 53, 2618–2626. https://doi.org/10.1002/2016WR020175.
FAO, 2020. WaPOR database methodology. Version 2 release, April 2020, 1st ed. FAO, Rome, Italy https://doi.org/10.4060/ca9894en.
Fisher, J.B., Lee, B., Purdy, A.J., Halverson, G.H., Dohlen, M.B., Cawse-Nicholson, K., Wang, A., Anderson, R.G., Aragon, B., Arain, M.A., Baldocchi, D.D., Baker, J.M., Barral, H., Bernacchi, C.J., Bernhofer, C., Biraud, S.C., Bohrer, G., Brunsell, N., Cappelaere, B., Castro-Contreras, S., Chun, J., Conrad, B.J., Cremonese, E., Demarty, J., Desai, A.R., Ligne, A.D., Foltýnová, L., Goulden, M.L., Griffis, T.J., Grünwald, T., Johnson, M.S., Kang, M., Kelbe, D., Kowalska, N., Lim, J.-H., Maïnassara, I., McCabe, M.F., Missik, J.E.C., Mohanty, B.P., Moore, C.E., Morillas, L., Morrison, R., Munger, J.W., Posse, G., Richardson, A.D., Russell, E.S., Ryu, Y., Sanchez-Azofeifa, A., Schmidt, M., Schwartz, E., Sharp, I., Šigut, L., Tang, Y., Hulley, G., Anderson, M., Hain, C., French, A., Wood, E., Hook, S., 2020. ECOSTRESS: NASAs next generation mission to measure evapotranspiration from the International Space Station. Water Resour. Res. 56, e2019WR026058. https://doi.org/10.1029/2019WR026058.
Funk, C., Peterson, P., Landsfeld, M., Pedreros, D., Verdin, J., Shukla, S., Husak, G., Rowland, J., Harrison, L., Hoell, A., Michaelsen, J., 2015. The climate hazards infrared precipitation with stations — a new environmental record for monitoring extremes. Sci. Data 2, 150066. https://doi.org/10.1038/sdata.2015.66.
Funk, C., Shukla, S., Thiaw, W.M., Rowland, J., Hoell, A., McNally, A., Husak, G., Novella, N., Budde, M., Peters-Lidard, C., Adoum, A., Galu, G., Korecha, D., Magadzire, T., Rodriguez, M., Robjhon, M., Bekele, E., Arsenault, K., Peterson, P., Harrison, L., Fuhrman, S., Davenport, F., Landsfeld, M., Pedreros, D., Jacob, J.P., Reynolds, C., Becker-Reshef, I., Verdin, J., 2019. Recognizing the famine early warning systems network: over 30 years of drought early warning science advances and partnerships promoting global food security. Bull. Am. Meteorol. Soc. 100, 1011–1027. https://doi.org/10.1175/BAMS-D-17-0233.1.
Gachene, C.K., Pearce, F., Leitner, S., Paliwal, A., Quinton, J., Rufino, M., 2025. Soils of ILRI'S Kapiti Research Station and Wildlife Conservancy.
García, M., Sandholt, I., Ceccato, P., Ridler, M., Mougin, E., Kergoat, L., Morillas, L., Timouk, F., Fensholt, R., Domingo, F., 2013. Actual evapotranspiration in drylands derived from in-situ and satellite data: assessing biophysical constraints. Remote Sens. Environ. 131, 103–118. https://doi.org/10.1016/j.rse.2012.12.016.
Hirschi, M., Michel, D., Lehner, I., Seneviratne, S.I., 2017. A site-level comparison of lysimeter and eddy covariance flux measurements of evapotranspiration. Hydrol. Earth Syst. Sci. 21, 1809–1825. https://doi.org/10.5194/hess-21-1809-2017.
Hobbins, M.T., Wood, A., McEvoy, D.J., Huntington, J.L., Morton, C., Anderson, M., Hain, C., 2016. The evaporative demand drought index. Part i: linking drought evolution to variations in evaporative demand. J. Hydrometeorol. 17, 1745–1761. https://doi.org/10.1175/JHM-D-15-0121.1.
Hu, T., Mallick, K., Hitzelberger, P., Didry, Y., Boulet, G., Szantoi, Z., Koetz, B., Alonso, I., Pascolini-Campbell, M., Halverson, G., Cawse-Nicholson, K., Hulley, G.C., Hook, S., Bhattarai, N., Olioso, A., Roujean, J.-L., Gamet, P., Su, B., 2023. Evaluating European ECOSTRESS hub evapotranspiration products across a range of soil-atmospheric aridity and biomes over Europe. Water Resour. Res. 59, e2022WR034132. https://doi.org/10.1029/2022WR034132.
Impens, I., Lemeur, R., 1969. Extinction of net radiation in different crop canopies. Arch. Für Meteorol. Geophys. Bioklimatol. Ser. B 17, 403–412. https://doi.org/10.1007/BF02243377.
Jacquemoud, S., 1993. Inversion of the PROSPECT+SAIL canopy reflectance model from AVIRIS equivalent spectra: theoretical study. Remote Sens. Environ. 44, 281–292.
Jasechko, S., Sharp, Z.D., Gibson, J.J., Birks, S.J., Yi, Y., Fawcett, P.J., 2013. Terrestrial water fluxes dominated by transpiration. Nature 496, 347–350. https://doi.org/10.1038/nature11983.
Javadian, M., Aubrecht, D.M., Fisher, J.B., Scott, R.L., Burns, S.P., Diehl, J.L., Munger, J. W., Richardson, A.D., 2024. Scaling individual tree transpiration with thermal cameras reveals interspecies differences to drought vulnerability. Geophys. Res. Lett. 51, e2024GL111479. https://doi.org/10.1029/2024GL111479.
Lian, X., Piao, S., Chen, A., Huntingford, C., Fu, B., Li, L.Z.X., Huang, J., Sheffield, J., Berg, A.M., Keenan, T.F., McVicar, T.R., Wada, Y., Wang, X., Wang, T., Yang, Y., Roderick, M.L., 2021. Multifaceted characteristics of dryland aridity changes in a warming world. Nat. Rev. Earth Environ. 2, 232–250. https://doi.org/10.1038/s43017-021-00144-0.
Liang, L., Feng, Y., Wu, J., He, X., Liang, S., Jiang, X., de Oliveira, G., Qiu, J., Zeng, Z., 2022. Evaluation of ECOSTRESS evapotranspiration estimates over heterogeneous landscapes in the continental US. J. Hydrol. 613, 128470. https://doi.org/10.1016/j.jhydrol.2022.128470.
Marshall, M., Funk, C., Michaelsen, J., 2012. Examining evapotranspiration trends in Africa. Clim. Dyn. 38, 1849–1865. https://doi.org/10.1007/s00382-012-1299-y.
Marshall, M., Tu, K., Funk, C., Michaelsen, J., Williams, P., Williams, C., Ardö, J., Boucher, M., Cappelaere, B., de Grandcourt, A., Nickless, A., Nouvellon, Y., Scholes, R., Kutsch, W., 2013. Improving operational land surface model canopy evapotranspiration in Africa using a direct remote sensing approach. Hydrol. Earth Syst. Sci. 17, 1079–1091. https://doi.org/10.5194/hess-17-1079-2013.
Marshall, M., Thenkabail, P., Biggs, T., Post, K., 2016. Hyperspectral narrowband and multispectral broadband indices for remote sensing of crop evapotranspiration and its components (transpiration and soil evaporation). Agric. For. Meteorol. 218–219, 122–134. https://doi.org/10.1016/j.agrformet.2015.12.025.
Marshall, M., Tu, K., Andreo, V., 2020. On parameterizing soil evaporation in a direct remote sensing model of ET: PT-JPL. Water Resour. Res. 56, e2019WR026290. https://doi.org/10.1029/2019WR026290.
Marshall, M., Belgiu, M., Boschetti, M., Pepe, M., Stein, A., Nelson, A., 2022. Field-level crop yield estimation with PRISMA and sentinel-2. ISPRS J. Photogramm. Remote Sens. 187, 191–210. https://doi.org/10.1016/j.isprsjprs.2022.03.008.
McKee, 1993. The relationship of drought frequency and duration of time scales. In: Eighth Conf. Appl. Climatol. January Anaheim Calif, 1993, pp. 17–22.
McMillen, R.T., 1988. An eddy correlation technique with extended applicability to non-simple terrain. Bound.-Layer Meteorol. 43, 231–245. https://doi.org/10.1007/BF00128405.
Melton, F.S., Huntington, J., Grimm, R., Herring, J., Hall, M., Rollison, D., Erickson, T., Allen, R., Anderson, M., Fisher, J.B., Kilic, A., Senay, G.B., Volk, J., Hain, C., Johnson, L., Ruhoff, A., Blankenau, P., Bromley, M., Carrara, W., Daudert, B., Doherty, C., Dunkerly, C., Friedrichs, M., Guzman, A., Halverson, G., Hansen, J., Harding, J., Kang, Y., Ketchum, D., Minor, B., Morton, C., Ortega-Salazar, S., Ott, T., Ozdogan, M., ReVelle, P.M., Schull, M., Wang, C., Yang, Y., Anderson, R.G., 2022. OpenET: filling a critical data gap in water management for the western United States. JAWRA J. Am. Water Resour. Assoc. 58, 971–994. https://doi.org/10.1111/1752-1688.12956.
Michel, D., Jiménez, C., Miralles, D.G., Jung, M., Hirschi, M., Ershadi, A., Martens, B., McCabe, M.F., Fisher, J.B., Mu, Q., Seneviratne, S.I., Wood, E.F., Fernández-Prieto, D., 2016. The WACMOS-ET project – part 1: tower-scale evaluation of four remote-sensing-based evapotranspiration algorithms. Hydrol. Earth Syst. Sci. 20, 803–822. https://doi.org/10.5194/hess-20-803-2016.
Miralles, D.G., Jiménez, C., Jung, M., Michel, D., Ershadi, A., McCabe, M.F., Hirschi, M., Martens, B., Dolman, A.J., Fisher, J.B., Mu, Q., Seneviratne, S.I., Wood, E.F., Fernández-Prieto, D., 2016. The WACMOS-ET project – part 2: evaluation of global terrestrial evaporation data sets. Hydrol. Earth Syst. Sci. 20, 823–842. https://doi.org/10.5194/hess-20-823-2016.
Moncrieff, J.B., Massheder, J.M., de Bruin, H., Elbers, J., Friborg, T., Heusinkveld, B., Kabat, P., Scott, S., Soegaard, H., Verhoef, A., 1997. A system to measure surface fluxes of momentum, sensible heat, water vapour and carbon dioxide. J. Hydrol. HAPEX-Sahel 188–189, 589–611. https://doi.org/10.1016/S0022-1694(96)03194-0.
Moore, C.J., 1986. Frequency response corrections for eddy correlation systems. Bound.-Layer Meteorol. 37, 17–35. https://doi.org/10.1007/BF00122754.
Myneni, R.B., Williams, D.L., 1994. On the relationship between FAPAR and NDVI. Remote Sens. Environ. 49, 200–211. https://doi.org/10.1016/0034-4257(94)90016-7.
Norman, J.M., Kustas, W.P., Humes, K.S., 1995. Source approach for estimating soil and vegetation energy fluxes in observations of directional radiometric surface temperature. Agric. For. Meteorol. 77, 263–293. https://doi.org/10.1016/0168-1923(95)02265-Y. Thermal Remote Sensing of the Energy and Water Balance over Vegetation.
OCHA, 2023. Horn of Africa Drought Regional Humanitarian Overview & Call to Action. United Nations Office for the Coordination of Humanitarian Affairs.
Odongo, V., Leitner, S.M., Dowling, T.P.F., Gluecks, I., Jackowicz-Korczynski, M., Rinne, J., Wooster, M.J., Merbold, L., 2025. Contrasting carbon and water flux dynamics in an east African rangeland and cropland. J. Geophys. Res. Biogeosci. 130, e2024JG008623. https://doi.org/10.1029/2024JG008623.
Otkin, J.A., Anderson, M.C., Hain, C., Svoboda, M., 2014. Examining the relationship between drought development and rapid changes in the evaporative stress index. J. Hydrometeorol. 15, 938–956. https://doi.org/10.1175/JHM-D-13-0110.1.
Potter, C.S., Randerson, J.T., Field, C.B., Matson, P.A., Vitousek, P.M., Mooney, H.A., Klooster, S.A., 1993. Terrestrial ecosystem production: a process model based on global satellite and surface data. Glob. Biogeochem. Cycles 7, 811–841. https://doi.org/10.1029/93GB02725.
Prata, A.J., 1996. A new long-wave formula for estimating downward clear-sky radiation at the surface. Q. J. R. Meteorol. Soc. 122, 1127–1151. https://doi.org/10.1002/qj.49712253306.
Priestley, C.H.B., Taylor, R.J., 1972. On the assessment of surface heat flux and evaporation using large-scale parameters. Mon. Weather Rev. 100, 81–92. https://doi.org/10.1175/1520-0493(1972)100%3C0081:OTAOSH%3E2.3.CO;2.
Purdy, A.J., Fisher, J.B., Goulden, M.L., Colliander, A., Halverson, G., Tu, K., Famiglietti, J.S., 2018. SMAP soil moisture improves global evapotranspiration. Remote Sens. Environ. 219, 1–14. https://doi.org/10.1016/j.rse.2018.09.023.

Richter, R., Schlapfer, D., 2023. Atmospheric / Topographic Correction for Satellite Imagery (ATCOR-2/3 User Guide Version 9.5). DLR - German Aerospace Center, Wessling, Germany.

Richter, K., Timmermans, W.J., 2009. Physically based retrieval of crop characteristics for improved water use estimates. Hydrol. Earth Syst. Sci. 13, 663–674. https://doi.org/10.5194/hess-13-663-2009.

Ross, J., 1976. Radiative transfer in plant communities. In: Vegetation and the Atmosphere. Academic Press, London, United Kingdom, pp. 13–55.

Ruddick, K.G., Bialek, A., Brando, V.E., De Vis, P., Dogliotti, A.I., Doxaran, D., Goryl, P., Goyens, C., Kuusk, J., Spengler, D., Turpie, K.R., Vanhellemont, Q., 2024. HYPERNETS: a network of automated hyperspectral radiometers to validate water and land surface reflectance (380–1680 nm) from all satellite missions. Front. Remote Sens. 5. https://doi.org/10.3389/frsen.2024.1372085.

Scheffler, D., Hollstein, A., Diedrich, H., Segl, K., Hostert, P., 2017. AROSICS: an automated and robust open-source image co-registration software for multi-sensor satellite data. Remote Sens. 9, 676. https://doi.org/10.3390/rs9070676.

Sharifnezhadazizi, Z., Norouzi, H., Prakash, S., Beale, C., Khanbilvardi, R., 2019. A global analysis of land surface temperature diurnal cycle using MODIS observations. J. Appl. Meteorol. Climatol. https://doi.org/10.1175/JAMC-D-18-0256.1.

Twine, T.E., Kustas, W.P., Norman, J.M., Cook, D.R., Houser, P.R., Meyers, T.P., Prueger, J.H., Starks, P.J., Wesely, M.L., 2000. Correcting eddy-covariance flux underestimates over a grassland. Agric. For. Meteorol. 103, 279–300. https://doi.org/10.1016/S0168-1923(00)00123-4.

UNEP, 2008. Africa: Atlas of our Changing Environment. UN Environment Programme, Nairobi, Kenya.

Vickers, D., Mahrt, L., 1997. Quality control and flux sampling problems for tower and aircraft data. J. Atmos. Ocean. Technol. 14, 512–526. https://doi.org/10.1175/1520-0426(1997)014%3C0512:QCAFSP%3E2.0.CO;2.

Wang, J., Dai, A., Mears, C., 2016. Global water vapor trend from 1988 to 2011 and its diurnal asymmetry based on GPS, radiosonde, and microwave satellite measurements. J. Clim. 29, 5205–5222. https://doi.org/10.1175/JCLI-D-15-0485.1.

Webb, E.K., Pearman, G.I., Leuning, R., 1980. Correction of flux measurements for density effects due to heat and water vapour transfer. Q. J. R. Meteorol. Soc. 106, 85–100. https://doi.org/10.1002/qj.49710644707.

Wen, J., Tagliabue, G., Rossini, M., Fava, F.P., Panigada, C., Merbold, L., Leitner, S., Sun, Y., 2025. Detection of fast-changing intra-seasonal vegetation dynamics of drylands using solar-induced chlorophyll fluorescence (SIF). Biogeosciences 22, 2049–2067. https://doi.org/10.5194/bg-22-2049-2025.

West, H., Quinn, N., Horswell, M., 2019. Remote sensing for drought monitoring & impact assessment: progress, past challenges and future opportunities. Remote Sens. Environ. 232, 111291. https://doi.org/10.1016/j.rse.2019.111291.

Wilson, K., Goldstein, A., Falge, E., Aubinet, M., Baldocchi, D., Berbigier, P., Bernhofer, C., Ceulemans, R., Dolman, H., Field, C., Grelle, A., Ibrom, A., Law, B.E., Kowalski, A., Meyers, T., Moncrieff, J., Monson, R., Oechel, W., Tenhunen, J., Valentini, R., Verma, S., 2002. Energy balance closure at FLUXNET sites. Agric. For. Meteorol. 113, 223–243. https://doi.org/10.1016/S0168-1923(02)00109-0. FLUXNET 2000 synthesis.

Zhang, L., Marshall, M., Nelson, A., Vrieling, A., 2021. A global assessment of PT-JPL soil evaporation in agroecosystems with optical, thermal, and microwave satellite data. Agric. For. Meteorol. 306, 108455. https://doi.org/10.1016/j.agrformet.2021.108455.

Zhang, H., Mahmood, A.N., Hu, T., Mallick, K., Didry, Y., Hitzelberger, P., Szantoi, Z., Pérez-Planells, L., Göttsche, F.M., Hulley, G.C., Hook, S.J., 2025. Global evaluation of high-resolution ECOSTRESS land surface temperature and emissivity products: collection 1 versus collection 2. Remote Sens. Environ. 326, 114799. https://doi.org/10.1016/j.rse.2025.114799.

Zhou, S., Williams, A.P., Berg, A.M., Cook, B.I., Zhang, Y., Hagemann, S., Lorenz, R., Seneviratne, S.I., Gentine, P., 2019. Land–atmosphere feedbacks exacerbate concurrent soil drought and atmospheric aridity. Proc. Natl. Acad. Sci. 116, 18848–18853. https://doi.org/10.1073/pnas.1904955116.

Zhou, Y., Sühring, M., Li, X., 2023. Evaluation of energy balance closure adjustment and imbalance prediction methods in the convective boundary layer – a large eddy simulation study. Agric. For. Meteorol. 333, 109382. https://doi.org/10.1016/j.agrformet.2023.109382.